General potential-energy function for H/Ni and dynamics calculations of surface diffusion, bulk diffusion, subsurface-to-surface transport, and absorption

Steven E. Wonchoba and Donald G. Truhlar

Department of Chemistry and Supercomputer Institute, University of Minnesota, Minneapolis, Minnesota 55455-0431

We present a potential-energy function for H interacting with bulk metallic Ni. The potential is parametrized to be accurate both for H adsorbed on Ni surfaces and for H absorbed at interior sites. The function introduces a nonlocal density dependence into the embedded-atom method formalism. We show that the function provides dramatic improvement over the best previous embedded-atom potential function for this system, and that it gives good agreement with all available structural and energetic data characterizing stationary points on the low-index surface planes [(100), (111), and (110)] and in the interior. It also yields good agreement with experiment for most diffusion coefficients and activation energies for surface and interior diffusion. We examine the dynamics of three diffusion processes: H diffusing on the (100) and (111) crystal faces, and H migrating in the interior, for the latter of which we analyze the reaction path and predict coefficients for H diffusion between adjacent interior octahedral vacancies. We also examine two other processes: H hopping from the threefold (111) surface binding site to an octahedral vacancy immediately beneath the (111) surface plane to (absorption), and the reverse process (deabsorption). We also calculate the binding energy and frequencies for H adsorbed on the pseudothreefold site of the Ni(110) surface, and we find them to be in good agreement with experiment and a considerable improvement over previous versions of the potential function. Our potential-energy function should be useful for simulations of a variety of processes that are difficult to study experimentally, such as surface diffusion in the presence of steps and kinks, site-to-site movement of H immediately beneath a surface plane of Ni, or bulk transport across a grain boundary.

I. INTRODUCTION

The development of useful potential-energy functions (PEF's) for atomic and molecular phenomena associated with interfaces and for atomic processes in the interior of catalytic and energy storing materials is of great current interest. Gas-metal interfaces provide strong challenges to theory in this regard, because the properties of a metal cannot adequately be reproduced by the popular models of pairwise forces and clusters.[1] However, the embedded-atom method (EAM) (Refs. 2–6) has had considerable success with modeling the interaction of an atom with a bulk metal. It has been less widely used for interfacial problems, but for H/Ni systems it has been used to model both surface and interior processes.[2,3,7–10] In recent work,[10] we presented an EAM-based PEF for H atoms interacting with the (100) crystal face of Ni that accurately reproduces experimental binding energies, hydrogenic vibrational frequencies, and equilibrium interatomic distances for H adsorbed at a fourfold equilibrium site, as well as activation energies and surface diffusion coefficients. We noted that although that PEF, called EAM5 because it is the fifth H/Ni EAM parameter set known to us, is very accurate for the (100) face of Ni, it is not particularly well suited for studying H diffusion on Ni(111) or for H diffusion in interior Ni. The goal of the work presented here is to create a general PEF for the H/Ni system that reproduces a wider range of the experimentally available system attributes, including both surface and interior interaction energies. The resulting parameter set will be called EAM6.

It is desirable to have such a more general H/Ni PEF for two reasons. In the first place, we are likely to have more faith in a semiempirical PEF that is based on an extensive and varied set of experimental data. Second, a general PEF will allow one to make calculations for conditions that are difficult to study in isolation by experimental techniques, e.g., surface diffusion at defects, steps, or kinks, subsurface H diffusion immediately below the Ni surface plane, or interior diffusion near defects or grain boundaries. Such situations cannot be treated with a PEF whose parameters are appropriate only for a specific crystal face. A PEF that accurately models the energetics for an H atom in several distinct environments on and in Ni is more likely to be reliable for calculations in which the H atom is in irregular surroundings that are different from those for which calibration data are available. If our PEF is accurate for surface processes on more than one face, in which the H atom is in a variety of low-electron-density environments, and for interior processes, in which the H atom is in various high-electron-density environments, then we are more likely to have faith in the results that it predicts for processes occurring in less well-characterized environments, such as subsurface processes, for which the H atom is in a moderate-to-high-electron-density environment. The potential catalytic activity of Ni makes the analysis of subsurface processes especially important for this system. It has been proposed by Maynard *et al.*[11] that the Ni surface catalyzed reaction of methyl radical with H to form CH_4 likely proceeds via a mechanism in which the CH_3 radical rests in a threefold minimum energy site on the Ni(111) surface, and the H atom attacks the radical from below the surface. This mechanism is suggested because CH_4 is not formed when CH_3 and H atoms are both adsorbed on the Ni surface, but it is formed when H is

53   11 222
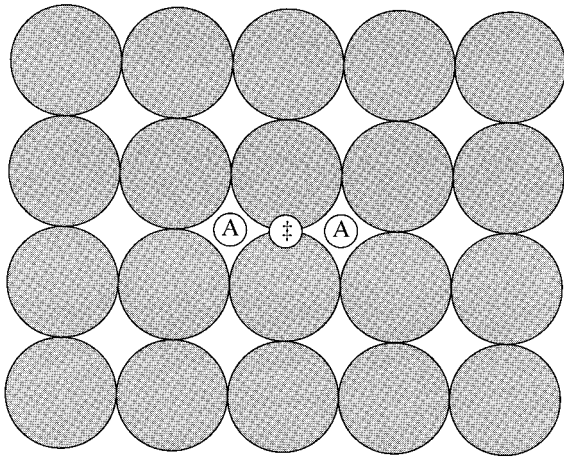
FIG. 1. Diagram of the Ni(100) crystal face. Two A_{100} sites are labeled A, and one $\ddagger_{100}$ site is labeled $\ddagger$.

present in the interior. The ability to model the energetics of subsurface H in Ni will provide more insight into this prototype catalytic process.

In this paper, Sec. II presents the methods used for dynamics and energetics calculations, describes the motivation for the fitting process, and presents our PEF. Section III presents calculations and results, Sec. IV analyzes and discusses the results, and Sec. V summarizes the conclusions.

II. THEORY

A. Sites

In this paper, we will examine the energetics and dynamics of hydrogen adsorption and diffusion on both the Ni(100) and Ni(111) crystal faces, hydrogen adsorption on Ni(110), hydrogen absorption and diffusion far beneath the surface in bulk Ni, and hydrogen absorption into the Ni(111) surface and the reverse process. In discussing the various stationary points (equilibrium binding sites and transition-state saddle points) for each case, we will make use of the following nomenclature. A minimum-energy site of adsorption is labeled A, followed by a subscript indicating the particular crystal face (100, 111, or 110). Minimum-energy interstitial absorption sites are labeled O_I for an octahedral interstitial vacancy or Te_I for a tetrahedral interstitial vacancy. Minimum-energy sites immediately beneath the Ni(111) surface are labeled $O_{S,111}$ for an octahedral subsurface interstitial vacancy and $Te_{S,111}$ for a tetrahedral subsurface interstitial vacancy. Saddle points are labeled $\ddagger$ followed by a subscript 100, 111, I, or S, the latter two indicating an interior site and a subsurface site, respectively.

For each of the surfaces, there are as many as three interesting stationary points. These sites are shown in Figs. 1–3. On the (100) crystal face, A_{100} is a surface cavity adsorption site formed by four adjacent (100) surface atoms, and $\ddagger_{100}$ is a bridging adsorption site between two A_{100} sites. The diffusion process consists of a particle moving from a fourfold A_{100} site through a twofold $\ddagger_{100}$ site to an adjacent A_{100} site. On the (111) surface, there are two distinct A_{111} sites. Both are in surface cavities formed by three adjacent (111) surface atoms, but one site is immediately above an atom in the
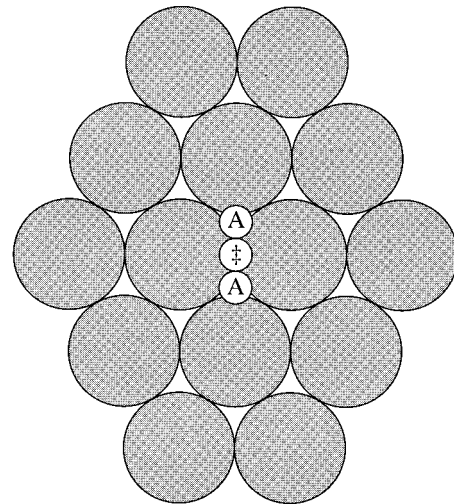
FIG. 2. Diagram of the Ni(111) crystal face. Two A_{111} sites are labeled A, and one $\ddagger_{111}$ site is labeled $\ddagger$.

second layer, and the other is immediately above a vacancy in the second layer. The diffusion process consists of a particle moving between these two distinct sites through a $\ddagger_{111}$ saddle point. Calculations with previous PEF's (Refs. 7, 8, and 10), as well as with the PEF presented in this paper, indicate that the binding energies [with respect to the energy of a H atom infinitely far from a Ni lattice with a clean exposed (111) surface] of the two distinct sites are within 0.01 kcal/mol of one another. Both the H-Ni nearest-neighbor distances and H distances above the (111) surface plane of the two sites are within 0.001 Å of one another. The frequencies of the H-atom vibration perpendicular to the surface plane are identical to within 1 cm^{-1} for the two sites, and the frequencies of the H-atom vibration parallel to the surface plane are identical to within 5 cm^{-1} for the two sites. Since all these quantities are nearly identical for both A_{111} sites, we do not distinguish between them. For adsorption on the (110) face, A_{110} is the pseudothreefold site formed by two surface plane Ni atoms and one second plane Ni atom. Two identical A_{110} sites are shown in Fig. 3.
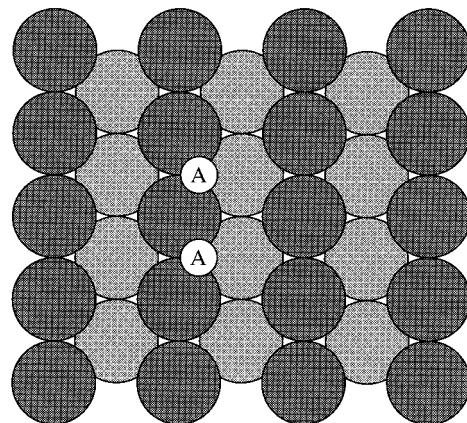
FIG. 3. Diagram of the first two atomic layers of the Ni(110) crystal face. Two A_{110} sites are labeled A.

STEVEN E. WONCHOBA AND DONALD G. TRUHLAR
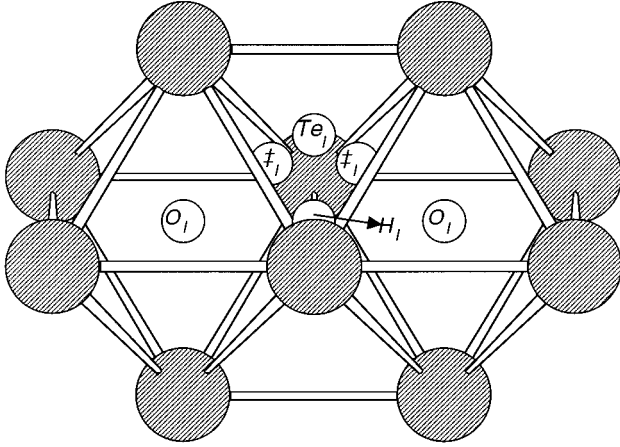
FIG. 4. Diagram of ten interior Ni atoms. The octahedral sites are labeled O_I, the saddle points are labeled $\ddagger_I$, the tetrahedral site is labeled Te_I, and the hilltop is labeled H_I. The minimum-energy reaction path is from one O_I site to the other O_I site passing through the two $\ddagger_I$ sites and the Te_I site.

For interior diffusion, four stationary points of interest are shown in Fig. 4. The complete interior diffusion process consists of a particle starting at an octahedral site O_I, moving through a saddle point, $\ddagger_I$, to a short-lived tetrahedral site Te_I, through another $\ddagger_I$ saddle point, and finally to another O_I site. This reaction path will be justified in Sec. IV. Another interior stationary point of interest is a second-order saddle point (a hilltop) directly joining the two adjacent I_O sites. This site is labeled H_I.

For (111) subsurface processes, by which we mean processes that involve sites *immediately* below the Ni(111) surface plane and for (111) absorption and deabsorption processes, by which we mean passage from the A_{111} adsorption site to such a subsurface site (and vice versa), the stationary points of interest are simply lower-symmetry versions of the interior stationary points. Ni atoms extend beyond the potential cutoff in all directions from the interior stationary points; however, the subsurface stationary points are not symmetric in the z direction (i.e., the direction perpendicular to the surface plane). As a result, while the O_I site has a triply degenerate H-atom vibration, the $O_{S,111}$ site has a doubly degenerate vibration (the two vibrations parallel to the surface plane) and a nondegenerate vibration (the vibration perpendicular to the surface plane). In general, the binding energy of a H atom absorbed at a subsurface site is slightly lower than that of an H atom absorbed at its interior analog.

There is one stationary point associated with absorption and deabsorption that does not have a direct analog to an interior site. Specifically, the saddle point for the surface-to-subsurface absorption process and the subsurface-to-surface deabsorption process has an H atom approximately coplanar with three adjacent (111) surface atoms. The local nearest-neighbor geometry of this saddle point is analogous to the $\ddagger_I$ site, but rather than bridging an O_I site and a Te_I site, it bridges an A_{111} site with either an $O_{S,111}$ site or a $Te_{S,111}$ site. To distinguish this important site, we label it $\ddagger_{Ab,111}$, where the subscript (Ab,111) indicates absorption into the lattice from the (111) surface. As with the A_{111} site, there are two distinct $\ddagger_{Ab,111}$ sites distinguished by the presence or absence

Ni (111) surface

Ni interior
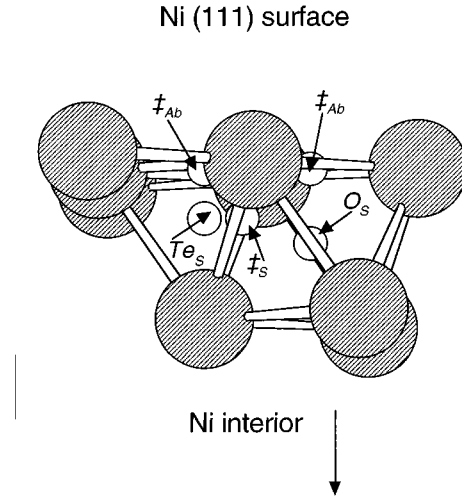
FIG. 5. Diagram of the subsurface sites for Ni(111). The $O_{S,111}$ and $Te_{S,111}$ sites are labeled O_S and Te_S, the $\ddagger_{S,111}$ site is labeled $\ddagger_S$, and the $\ddagger_{Ab,111}$ site is labeled $\ddagger_{Ab}$.

of a Ni atom in the second atomic layer. We will show in Sec. IV that the $\ddagger_{Ab,111}$ site immediately above a vacancy in the second atomic layer is of substantially more practical importance than the one immediately above an atom in the second atomic layer. The stationary points of interest to the (111) subsurface processes are shown in Fig. 5. Note that if the Ni lattice were not terminated by the (111) surface, the $O_{S,111}$ and $Te_{S,111}$ sites would be O_I and Te_I sites, and the $\ddagger_{S,111}$ and $\ddagger_{Ab,111}$ sites would be $\ddagger_I$ sites. In addition to the three elementary diffusion processes discussed above, we also examine both the hydrogen absorption process from A_{111} to $O_{S,111}$, and the reverse of this process.

B. Dynamics

In the present paper, we approximate the site-to-site hopping rate constants $k(T)$ of the five processes outlined above [diffusion on (100), diffusion on (111), diffusion in the interior, absorption, and deabsorption] by canonical variational transition-state theory[12–17] (CVT) with a small curvature tunneling approximation[18] based on quantized reactant states[10,19] (SCTQ). For the three macroscopic diffusion processes, these hopping rate constants are converted to diffusion coefficients by[20]

$$D(T) = \frac{\lambda^2}{2d} k(T), \qquad (1)$$

where T is temperature, λ is the distance between reactant and product minimum-energy sites, and d is the dimensionality of the process. Table I gives the values of λ and d used for (100) diffusion, (111) diffusion, and interior diffusion. The absorption process and its reverse are not diffusion processes (because they do not correspond to mechanisms for transport over macroscopic dimensions), but rather are specific monatomic hops for which we only calculate $k(T)$. We next discuss the features of the CVT/SCTQ method, which are important to understand the calculations of $k(T)$ for all five processes.

TABLE I. Hop length (λ) in terms of the lattice constant ($R_0 = 3.52$ Å), dimensionality (d), and symmetry factor (σ) for H diffusion on Ni(100) and Ni(111) and in interior Ni.

Process	λ	d	σ
H/Ni(100) surface diffusion	$R_0/\sqrt{2}$	2	4
H/Ni(111) surface diffusion	$\sqrt{6}R_0/6$	2	3
H/Ni interior diffusion	$R_0/\sqrt{2}$	3	8

All dynamics calculations (as well as characterizations of stationary points) are carried out by the embedded-cluster method described previously.[10,17,21] In this method, the metal atoms allowed to move in each crystal lattice were chosen as those which are within a certain distance of the important stationary points for a diffusion process at that surface or in the interior of the crystal. This region of moving atoms is called the primary zone. The primary zone is made as large as necessary to yield converged energetics and dynamics. Surrounding the primary zone is a set of rigid atoms which extends far enough to include all atoms that are within the potential cutoff distance to all atoms in the primary zone. This surrounding set of atoms is called the secondary zone. In Sec. III we discuss in more detail the primary and secondary zones for each system studied, and we evaluate the convergence of the energetics and dynamics with respect to the size of the primary zone.

To calculate a CVT rate constant, we consider a representative reaction path, which we take to be the minimum-energy path (MEP) through the saddle point of interest. Each MEP is calculated as the path of steepest descents[14,22,23] in the mass-scaled Cartesian coordinates[24–28] of the adsorbate and primary-zone metal atoms on the potential-energy surface from the saddle point of the surface. We define a reaction coordinate s along the MEP. In the present work, the coordinates are scaled to a mass of 1 amu. At the saddle point, $s = 0$; at the reactant, $s = s^R$ (where s^R is a finite negative number for the unimolecular reactions considered here); and at the product, $s = s^P$ (where s^P is a finite positive number). The specific value of s^R for a particular minimum-energy site depends on the process. In the present paper, $s^R(A_{100})$ denotes the value of s at the A_{100} minimum-energy site, $s^R(O_I)$ denotes the value of s at the interior octahedral site, $s^R(Te_I)$ denotes the value of s at the interior tetrahedral site, etc. Next, the dynamical bottleneck is chosen from among a series of dividing surfaces (called generalized transition states) orthogonal to the MEP as the one which minimizes recrossing effects[12–17] and therefore minimizes the rate constant. The upper limit to the CVT rate constant is the conventional transition-state theory (TST) rate constant, which always uses the dividing surface which passes through the saddle point as the dynamical bottleneck. In cases where this is the true dynamical bottleneck, the CVT rate constant is equal to the TST rate constant. We will show in Sec. III that variational effects are very important for some of the processes (particularly interior and subsurface processes) studied here, and that the CVT method provides a better approximation to the classical rate constant. That is, the true dynamical bottleneck does not always pass through the saddle point.

Quantum-mechanical effects are incorporated into the rate constant by making a separable mode approximation, quantizing the partition functions associated with the adsorbate and primary-zone atoms of the reactant and the transition state, and then multiplying by a factor that accounts for tunneling along the reaction path from bound reactant states using a small-curvature-tunneling (SCT), quantized-reactant (Q) approximation. The resulting expression for the rate constant is

$$k^{\text{CVT/SCTQ}}(T) = \kappa^{\text{CVT/GQ}}(T)\frac{\sigma k_B T}{h}\frac{Q^{\text{CVT}}(T)}{Q^R(T)}$$
$$\times \exp\left(\frac{-V_{\text{MEP}}^{\text{CVT}}(T)}{k_B T}\right), \tag{2}$$

where the superscript on $k(T)$ indicates the level of theory used to calculate the rate constant, $\kappa^{\text{CVT/GQ}}(T)$ is the ground-state transmission coefficient with quantized reaction-coordinate states described in Refs. 10 and 19, k_B is Boltzmann's constant, h is Planck's constant, $Q^{\text{CVT}}(T)$ and $Q^R(T)$ are the quantized partition functions of the transition state and reactant sites, respectively, $V_{\text{MEP}}^{\text{CVT}}(T)$ is the Born-Oppenheimer potential energy of the system at the dynamical bottleneck, and σ is a symmetry factor equal to the number of equivalent pathways from the reactant site to a product site. This number is equal to the coordination number of the reactant divided by the coordination number of the transition state. Table I lists the values of σ for the three diffusion processes considered here. For the absorption and deabsorption processes, σ is equal to 1. An approximation to the SCTQ method is to treat the reaction-coordinate energy levels as a classical continuum (i.e., rather than quantizing them). This latter approximation[10,18] is denoted SCT, CVT/SCT, and CVT/G, all without the Q.

The effective potential used for tunneling is the vibrationally adiabatic ground-state potential-energy curve, given by[26]

$$V_a^G(s) = V_{\text{MEP}}(s) + \varepsilon_{\text{trans}}^G(s) \tag{3}$$

where $V_{\text{MEP}}(s)$ is the potential energy at a point s along the MEP, and $\varepsilon_{\text{trans}}^G(s)$ is the ground-state vibrational energy of all adsorbate and primary-zone modes transverse to the reaction path. Both $\varepsilon_{\text{trans}}^G(s)$ and the energy levels required to calculate $Q^{\text{CVT}}(T)$ are calculated in the Cartesian coordinate harmonic approximation explained elsewhere.[14] At this point, we define two useful quantities. For hydrogen diffusion on or in a Ni lattice with N Ni atoms in the primary zone, there are $F = 3(N+1)$ vibrations. One of these vibrations is associated with reaction path motion, and this leaves $M = F - 1$ vibrations transverse to the reaction path. When the variational transition state is at $s = 0$, then the vibrationally adiabatic barrier height is given by

$$\Delta V_a^{\ddagger G} = V_a^G(s=0) - V_a^G(s=s^R), \tag{4}$$

which in the harmonic approximation is equal to

$$\Delta V_a^{\ddagger G} = \left[E(\ddagger) + \tfrac{1}{2}\sum_{m=1}^{M} hc\bar{\nu}_m^{\ddagger}\right] - \left[E(R) + \tfrac{1}{2}\sum_{m=1}^{M} hc\bar{\nu}_m^{R}\right], \tag{5}$$

where c is the speed of light, $E(R)$ and $E(\ddagger)$ are the Born-Oppenheimer energies of the minimum energy and saddle-point sites, $\bar{v}_m^R$ are frequencies in wave numbers of the M modes transverse to the reaction path mode associated with the minimum-energy site, and $\bar{v}_m^{\ddagger}$ are frequencies in wave numbers of the transverse modes associated with the saddle point. Subtracting the zero-point energy of the reaction path mode at the reactant site from Eq. (5) gives the zero-point corrected barrier height, which we call $\Delta E_0^{\ddagger}$. Note that $E(\ddagger) - E(R)$ is called the classical barrier height.

The activation energy E_a, in contrast to $\Delta V_a^{\ddagger G}$ and $\Delta E_0^{\ddagger}$, is defined in terms of dynamical properties and depends on temperature; in particular,[29]

$$E_a(T) = -RT \frac{d \ln(k)}{d(1/T)}. \tag{6}$$

However, in previous work[10] we have found that if the maximum of the vibrationally adiabatic curve is at $s = 0$, then $\Delta E_0^{\ddagger}$ gives a reasonable estimation of the high-temperature activation energy for the diffusion process, i.e.,

$$E_a(\text{high } T) \approx \Delta E_0^{\ddagger}. \tag{7}$$

In practice, since the activation energy depends on temperature, one must be careful about consistency when comparing theory to experiment. In Sec. IV, when carrying out such comparisons, we fit both theory and experiment at the same two temperatures to the form

$$D(T) = D_0 \exp\left(-\frac{E_a}{RT}\right) \tag{8a}$$

for the three diffusion processes and to

$$k(T) = A \exp\left(-\frac{E_a}{RT}\right) \tag{8b}$$

for the absorption and deabsorption processes. These two definitions of E_a are consistent, since the other factors in Eq. (1) are independent of temperature.

C. Potential-energy function

We now present the EAM potential, to be called EAM6, that is used in the current work. In previous work,[2,3,7–10] potential functions were created using the standard EAM formalism presented by Daw and Baskes.[2] In this formalism, the energy V_α of an atom α is given as

$$V_\alpha = F_\alpha(\bar{\rho}_\alpha) + \frac{1}{2} \sum_{\alpha \neq \alpha'} \phi(R_{\alpha\alpha'}), \tag{9}$$

and the energy of the entire system is given as

$$V = \sum_\alpha V_\alpha. \tag{10}$$

In the above equations, $F_\alpha(\bar{\rho}_\alpha)$ is the energy to embed atom α into a system at a point where the surrounding electron density $\bar{\rho}_\alpha$ is the sum of the individual atomic electron densities, $\bar{\rho}_{\alpha'}^a$, contributed by all other atoms, α', in the system at the point where atom α is to be embedded, i.e.,

$$\bar{\rho}_\alpha \equiv \sum_{\alpha'} \bar{\rho}_{\alpha'}^a. \tag{11}$$

The second term in Eq. (9) involves a sum of the pair potentials between atom α and all other atoms α' in the system, where $R_{\alpha\alpha'}$ is the interatomic distance between atom α and atom α'. The first term in Eq. (9) includes nonpairwise, many-body interactions, which are known[1] to be an essential ingredient for a PEF to model metallic systems accurately.

The calculation of the density, Eq. (11), in the current work is identical to that in EAM5, and specific details of this calculation are given in previous work.[2,9,10] The specific functional forms of the Ni and H embedding functions [i.e., $F_{\text{Ni}}(\bar{\rho}_\alpha)$ and $F_{\text{H}}(\bar{\rho}_\alpha)$ in Eqs. (9) and (10)] and of the pair potential will be presented below.

As mentioned above, EAM5 is not particularly well suited for H in an interior interstitial site in Ni. In particular, although vibrational frequencies and energetics for H absorbed at interior stationary points are given quite accurately, for pure Ni EAM5 predicts elastic constants and a bulk modulus that are too low, and it yields an inaccurate Cauchy discrepancy.[2,10] The first step in the reparametrization was to correct these problems. Since these problems do not involve H interaction with Ni, they could be fixed by adjusting only the Ni parameters.

1. Ni parameters

We assumed the same Coulombic form of the repulsive pair potential given by Daw and Baskes[2] and used in previous versions of the current EAM potential:

$$\phi(R_{\alpha\alpha'}) = \frac{C Z_\alpha(R_{\alpha\alpha'}) Z_{\alpha'}(R_{\alpha\alpha'})}{R_{\alpha\alpha'}}, \tag{12}$$

where C is a constant equal to 14.3888 eV Å, and $Z_\alpha(R_{\alpha\alpha'})$ and $Z_{\alpha'}(R_{\alpha\alpha'})$ are the effective nuclear charges of atoms α and α' at a distance $R_{\alpha\alpha'}$ from the nuclei. These functions are cut off to zero at a finite range with continuous first and second derivatives by incorporating a smoothing function which is given in Refs. 8 and 10. We used the same $Z_{\text{Ni}}(R_{\alpha\alpha'})$ used in previous[7,8,10] work:

$$Z_{\text{Ni}}(R_{\alpha\alpha'}) = Z_0 \left[1 + \left(\frac{R_{\alpha\alpha'}}{b}\right)^c \right] \exp\left(\frac{-R_{\alpha\alpha'}}{a}\right). \tag{13}$$

The values a, b, and c are given in Table II.

Rose et al.[30] presented a universal energy function for Ni (as well as many other metals) depending upon the sublimation energy and a variable lattice constant. This function, along with Eqs. (9), (11), and (12), leads to a set of points to which the Ni embedding function can be fit. Previous functional forms[7,8,10] of the Ni embedding energy involved a sum of three exponentials to which we have been unable to fit the function and its first two derivatives precisely enough to yield both accurate elastic constants and an accurate lattice constant. In EAM6, we therefore expand the fit to a sum of four exponentials, and we fit the embedding energy over the region $0 < \bar{\rho}_\alpha \leq 0.1$ Å^{-3}. Above $\bar{\rho}_\alpha = 0.1$ Å^{-3}, we introduced a quintic spline with continuous first and second derivatives which force the function to equal a constant value at large $\bar{\rho}_\alpha$. The resulting Ni embedding function is given as

TABLE II. EAM6 parameter set.

Function	Parameters			
Z_{Ni}	$Z_0 = 10.0$	$a = 0.537$ Å	$b = 1.116$ Å	$c = 1.0$
Z_H	$a_1 = 0.374$ Å	$b_1 = 0.932$ Å	$c_1 = 2.775$	$d_1 = 0.007\,52$
	$a_2 = 0.010$ Å	$b_2 = 0.549$ Å	$c_2 = 142.678$	$d_2 = 8.0036$ Å^{-1}
	$a_3 = 0.011$ Å	$b_3 = 0.377$ Å	$c_3 = 95.455$	$d_3 = 2.401$ Å
F_{Ni}	$A_{Ni} = -303.289$ eV Å^3	$B_{Ni} = 87.987$ eV$^{1/3}$ Å^3	$C_{Ni} = -522.774$ eV Å^3	$D_{Ni} = 39.421$ eV$^{1/5}$ Å^3
	$\alpha_{Ni} = 7.647$ Å^3	$\beta_{Ni} = 75.075$ Å^3	$\gamma_{Ni} = 373.379$ Å^3	$\delta_{Ni} = 56.342$ Å^3
	$A_s = -2.015 \times 10^{10}$ eV Å^{15}	$B_s = -5.384 \times 10^8$ eV Å^{12}	$C_s = -4.060 \times 10^6$ eV Å^9	$D_s = -11.031$ eV
	$\rho_c = 0.11$ Å^{-3}	$\Delta = 0.01$ Å^{-3}		
$F_H(\bar{\rho})$	$E_{H_1} = 476.121$ eV Å^3	$\varepsilon_{H_1} = 5.072$ Å^3	$E_{H_2} = -543.394$ eV Å^3	$\varepsilon_{H_2} = 5.285$ Å^3
$F_H(\hat{\rho}\alpha_1, \hat{\rho}\alpha_2)$	$Q_1 = 2$	$Q_2 = 0.5$		
	$\xi_{11} = -0.040\,84$ eV	$\xi_{12} = 3.686 \times 10^8$ Å^6	$\xi_{13} = 13\,563$ Å^{-6}	
	$\xi_{21} = -0.003\,25$ eV	$\xi_{22} = 54.772$ Å$^{3/2}$	$\xi_{23} = 0.812$ Å$^{-3/2}$	

$$F_{Ni}(\bar{\rho}_\alpha) = \begin{cases} A\exp(-\alpha_{Ni}\bar{\rho}_\alpha) + (B_{Ni}\bar{\rho}_\alpha)^3\exp(-\beta_{Ni}\bar{\rho}_\alpha) + C_{Ni}\exp(-\gamma_{Ni}\bar{\rho}_\alpha) + (D_{Ni}\bar{\rho}_\alpha)^5\exp(-\delta_{Ni}\bar{\rho}_\alpha), & 0 \leq \bar{\rho}_\alpha \leq \rho_c - \Delta \\ A_s(\bar{\rho}_\alpha - \rho_c)^5 + B_s(\bar{\rho}_\alpha - \rho_c)^4 + C_s(\bar{\rho}_\alpha - \rho_c)^3 + D_s, & \rho_c - \Delta \leq \bar{\rho}_\alpha \leq \rho_c \\ D_S, & \rho_c < \bar{\rho}_\alpha. \end{cases}$$

$$(14)$$

The parameters in Eq. (14) are given in Table II. We justify the simple treatment of the region with $\bar{\rho}_\alpha > 0.1$ Å^{-3} by the fact that in the processes examined in the present study, lattice atoms are never in surrounding densities greater than 0.07 Å^{-3}, and we note that for an interior Ni atom to be embedded in a vacancy with a surrounding atomic density of 0.1 Å^{-3}, the nearby lattice atoms would have to be compressed equivalently to a lattice constant of 3.29 Å [the equilibrium lattice constant is 3.52 Å (Ref. 31)].

Calculated bulk Ni characteristics with no H atom present are given in Table III, where they are compared to experiment.[32–37] We note that the bulk lattice quantities predicted by EAM6, in particular the elastic constants and bulk modulus, are in much better agreement with experiment than are those predicted by EAM5. Once the Ni parameters were

TABLE III. Energetically minimized lattice constant R_0, sublimation energy E_s, monovacancy formation energy $E_{1\nu}^F$, elastic constants, and bulk modulus B, calculated by EAM5 and EAM6 compared to experiment.

Quantity	Experiment	EAM5 [a]	EAM6
R_0 (Å)	3.52 [b]	3.5211	3.5235
E_s (eV)	4.45 [c]	4.43	4.46
$E_{1\nu}^F$ (eV)	1.39–1.70 [d]	1.66	1.63
C_{11} (10^{12} dyn/cm^2)	2.465 [e]	1.852	2.184
C_{12} (10^{12} dyn/cm^2)	1.473 [e]	1.238	1.560
C_{44} (10^{12} dyn/cm^2)	1.247 [e]	1.255	1.263
B (10^{12} dyn/cm^2)	1.86 [e]	1.44	1.77

[a]Reference 10.
[b]Reference 31.
[c]Reference 32.
[d]References 33–36.
[e]References 37.

determined, we prepared the final versions of the Ni lattices to be used in the calculations. We have demonstrated in previous work[21] the importance of using a lattice constant that is consistent with the assumed potential-energy function when constructing the metal lattices. For EAM6, the energetically minimized lattice constant R_0 is 3.5235 Å. Thus all Ni lattices in this work are constructed with this lattice constant. The lattices are discussed in detail in Sec. III.

2. H-Ni interaction parameters

The above step focused on the energetics of bulk Ni with no H atom present. Another area in which we improved EAM5 is the treatment of a H atom on the (111) surface. The experimental value[11] for the doubly degenerate hydrogenic vibration parallel to the (111) surface is 955 cm^{-1}, and EAM5 yields a value of 387 cm^{-1} for this quantity. Also, EAM5 leads to Arrhenius activation energies substantially lower (by about 2–3 kcal/mol) than experiment. These inaccuracies lead to questionable reaction dynamics and to diffusion coefficients which are nearly six orders of magnitude higher than experimental values.[38,39] The second step in the reparametrization was to improve the predicted energetics of a hydrogen atom interacting with the Ni(111) surface, while maintaining the good agreement of predicted features for the (100) surface. Given the EAM formalism discussed above, we considered several ways of doing this.

The first method is global reparametrization. This involves choosing a functional form and allowing all the parameters to vary in order to minimize the error with respect to all experimental quantities to which the function is being fit. In practice we found that this method only very minimally improves the (111) surface characteristics. In addition, since EAM5 is already very accurately parametrized for (100) surface calculations, global reparametrization to improve H on Ni(111) tends to introduce larger errors for H on

Ni(100), and these are not justifiable by the minimal improvement for (111).

Method 2 is local reparametrization. This involves making parameter changes that—as much as possible—only affect the stationary points whose characteristics we are interested in changing, specifically the vibrational frequencies at the A_{111} site and the activation energy for diffusion on the (111) crystal face. This is an attractive approach in principle, but in practice it only succeeds to a limited extent because several of the stationary points whose energetics are to be simultaneously addressed are very close to one another in the space of the independent variables. Thus, if one introduces a correction function that is active only in the offending region of the PEF, it needs to be so sharply varying that it tends to introduce fluctuations of the frequencies along the reaction paths. If, however, one introduces a smoother correction function, it tends to damage the accuracy of energetic predictions for other equilibrium or transition state sites. Although the fluctuation problem is not a serious one if the fluctuations are small, we found that attempts to make localized changes that are large enough to make the (111) diffusion barrier agree with experiment introduced severe fluctuations that led to an oscillating vibrationally adiabatic ground-state potential-energy curve [see Eq. (3)], which in turn leads to unphysical tunneling calculations. Although some improvement can be obtained with local modifications, we eventually concluded that it is necessary to increase the space of independent variables, and we did this by introducing a nonlocal density feature in the embedding function. The final strategy thus involved a combination of global, local, and nonlocal approaches, and these steps are discussed in more detail in the following paragraphs.

We first employed the global and local reparametrization schemes without extending either method so far that either oscillating vibrationally adiabatic ground-state potential-energy curves or significantly larger errors on (100) were introduced, and then we introduced nonlocal functional dependency to decrease the remaining error on (111). The functional form was introduced in $F_H(\bar{\rho}_\alpha)$, the embedding energy of the H atom, and we simultaneously reparametrized $Z_H(R_{\alpha\alpha'})$, the effective nuclear charge of the H atom, to reproduce as accurately as possible the frequencies and energetics associated with four of the surface stationary points mentioned in Sec. II A (A_{100}, $\ddagger_{100}$, A_{111}, and $\ddagger_{111}$).

For $Z_H(R_{\alpha\alpha'})$, we chose to use

$$Z_H(R_{\alpha\alpha'}) = \sum_{j=1}^{3} \left[\left(\frac{R_{\alpha\alpha'}}{b_j} \right)^{c_j} \exp\left(\frac{-R_{\alpha\alpha'}}{a_j} \right) \right]$$
$$+ d_1 \text{sech}[d_2(R_{\alpha\alpha'} - d_3)]. \quad (15)$$

The reasons for using this functional form are as follows. For all four surface stationary points used in the fit, 90–95 % of the H-Ni pair interaction is due to the nearest-neighbor contributions. As a result, the values of $Z_H(R_{\alpha\alpha'})$ and its first two derivatives at the nearest-neighbor distances must be the crux of any successful parametrization of Eq. (15). The summation of exponentials provides the degrees of freedom necessary to alter selectively the potential curve at the nearest-neighbor distances of the stationary points whose characteristics needed to be changed, while also providing a

smooth, well-behaved function, as is necessary to insure physically reasonable frequencies along the reaction paths and hence well-behaved V_a^G curves with no spurious artifacts. The second-nearest neighbors contribute most of the remaining pairwise interaction, with third- and further nearest neighbors contributing less than 1.1% of the interaction. The hyperbolic secant is specifically added in a region which almost exclusively affects the second-nearest-neighbor interaction of the $\ddagger_{111}$ site. This localized change allows an increase in the energy of the $\ddagger_{111}$ site [and, therefore, an increase in $\Delta E_0^\ddagger$ of the diffusion process on the (111) surface] without severely affecting the vibrational frequencies orthogonal to the reaction paths.

The H-atom embedding function has a much larger effect on the energies of the stationary points than on the frequencies. Therefore, the functional form of $F_H(\bar{\rho}_\alpha)$ was generalized to allow the embedding function to depend on additional combinations of the density contributions of the other atoms. In particular,

$$F_H(\bar{\rho}_\alpha, \hat{\rho}_\alpha^{(1)}, \hat{\rho}_\alpha^{(2)}) = \sum_{j=1}^{2} [E_{H_j} \bar{\rho}_\alpha \exp(\varepsilon_{H_j} \bar{\rho}_\alpha)]$$
$$+ \sum_{k=1}^{2} \xi_{k1} \text{sech}[\xi_{k2}(\hat{\rho}_\alpha^{(k)} - \xi_{k3})],$$
$$(16)$$

where

$$\hat{\rho}_\alpha^{(k)} = \sum_{\alpha'} (\bar{\rho}_{\alpha'}^a)^{Q_k}. \quad (17)$$

This is a computationally efficient way to introduce what would be equivalent to nonlocal corrections (gradient corrections) in density-functional theory. It is similar to the embedding functions used in previous work,[7,8,10] but in addition to being a function of the sum of individual electron densities created by all other atoms, it is also a function of the sum of the individual densities all taken to some power Q_1 and of their sum when taken to some other power Q_2. This function gives different embedding energies for two sites with approximately the same $\bar{\rho}_\alpha$, depending on whether that $\bar{\rho}_\alpha$ results from a larger number of smaller (and hence more slowly varying) density contributions or a smaller number of larger (and hence more rapidly varying) contributions. As a consequence, it more clearly distinguishes the regions of the PEF that affect the various stationary points, and it therefore allows us to make localized corrections to the function without damaging the already accurate regions.

To optimize the parameters of these functions, we first set ξ_{11} and ξ_{21} equal to zero, and use a variation of the simplex algorithm[40] to adjust the parameters of $Z_H(R_{\alpha\alpha'})$ and the first sum of Eq. (16) to minimize an error function relating the experimental (where available) energetics and frequencies of the four surface stationary points used in the fit to those predicted by the potential-energy function. The error function which was minimized is

$$S = \sum_{\alpha} W(\alpha) \left(\frac{\alpha_{\text{calc}} - \alpha_{\text{lit}}}{\alpha_{\text{lit}}} \right)^2. \quad (18)$$

where α represents an observable quantity, α_{calc} is the calculated value for that quantity, α_{lit} is a target experimental value or other theoretical value from the literature, and $W(\alpha)$ is a weighting function. The weighting function accounts for the difference in magnitude of the various quantities, and weights them according to the level of reliability of the literature data or the acceptable level of fitting accuracy for realistic dynamics calculations. In particular, the weighting function is defined as

$$W(\alpha) = \left[\alpha_{\text{lit}} \Big/ \left(\max \left\{ \begin{array}{c} \Delta \alpha_{\text{lit}} \\ \Delta \alpha_{\text{acc}} \end{array} \right\} \right) \right]^2, \qquad (19)$$

where $\Delta \alpha_{\text{lit}}$ is the reported error estimate in the literature value for the observable quantity α, and $\Delta \alpha_{\text{acc}}$ is the required level of accuracy for this quantity. Usually, $\Delta \alpha_{\text{acc}}$ equals $\Delta \alpha_{\text{lit}}$, unless no error estimate is given in the literature or if $\Delta \alpha_{\text{lit}}$ is much smaller than is necessary to obtain a good fit to the data.

The quantities used in the minimization of the error function and the corresponding quantities used in Eqs. (18) and (19) are given in Table IV. For the A_{100} and A_{111} sites, values for α_{lit} were taken from experiment.[11,38,39,41–57] Values for $\Delta \alpha_{\text{lit}}$ are either the error range given in the reference or the range of experimentally measured values for the given quantity. The α_{lit} values for the perpendicular hydrogenic vibrational frequency at the saddle points were obtained from theoretical calculations made for the $\ddagger_{100}$ site[55] and the $\ddagger_{111}$ site.[56] Since there are no experimental data for $E(\ddagger_{100})$ and $E(\ddagger_{111})$, we estimated α_{lit} values for these quantities at the fitting stage by assuming that the experimental activation energy at the highest available temperature range measured is well approximated by our calculated $\Delta E_0^{\ddagger}$ [see Eq. (7)]. This was a reasonable and practical way to proceed at the fitting stage, but in Sec. IV we will discuss alternative methods for approximating $E(\ddagger)$ values. These alternative methods are perhaps more reliable for $E(\ddagger_{111})$, because the highest temperature experiments available for the (111) surface may not be high enough to validate the assumption of Eq. (7).

The parameters for the effective nuclear charge on the H atom, Eq. (15), and the local part of the hydrogen embedding energy, the first sum in Eq. (16), were adjusted by approximately minimizing Eq. (18), and the parameters for the nonlocal part of the hydrogen-embedding function, the second sum in Eq. (16), were manually optimized. Table II lists the values of all of these parameters for EAM6.

The actual parametrization that we have just described was based on rigid-lattice calculations. We have shown[10] that the frequencies and energetics of H on the (100) crystal face do not depend very much on lattice motion. We also determined, through a brief study of the (111) face in the previous[10] work, that the same is true for H on the (111) crystal face. Since lattice motion has such a small effect on these quantities, it was not necessary to use nonrigid lattices during the parametrization stage. (The above conclusions were originally made from results calculated with EAM5, but we later found that calculations with EAM6 yield the same conclusions, as we will show in Sec. III.) Note that although parametrization was carried out with rigid lattices,

TABLE IV. Quantities used in the minimization of the error function Eq. (18) for the parametrization of Z_H and F_H. Energies E and zero-point-corrected barrier heights, $\Delta E_0^{\ddagger}$ are given in kcal/mol, equilibrium heights above the surface plane z are given in Å, and frequencies $\overline{\nu}$ are given in wave numbers. Values in parentheses are calculated.

α	α_{lit}	$\Delta \alpha_{\text{lit}}$	$\Delta \alpha_{\text{acc}}$	$W(\alpha)$
		(A_{100})		
E	-64.5 [a]	0.7 [a]	0.7	5152.0
z	0.5 [b]	0.1 [b]	0.1	25.0
$\Delta E_0^{\ddagger}$	4.0 [c]	0.9 [c]	0.9	19.8
$\overline{\nu}_{\perp}$	565 [d]	32 [d]	150	14.2
$\overline{\nu}_{\parallel}$	387 [e]		200	3.7
		$(\ddagger_{100})$		
$\overline{\nu}_{\perp}$	(1428) [f]		200	51.0
		(A_{111})		
E	-66.2 [g]	0.6 [g]	0.6	17 476.8
z	1.0 [h]	0.2 [h]	0.2	25.0
$\Delta E_0^{\ddagger}$	3.3 [i]	1.0 [i]	1.0	10.9
$\overline{\nu}_{\perp}$	1150 [j]	30 [j]	150	58.8
$\overline{\nu}_{\parallel}$	955 [k]		200	22.8
		$(\ddagger_{111})$		
$\overline{\nu}_{\perp}$	(1183) [l]		200	35.0

[a]Binding energies calculated from heats of adsorption (ΔH_T) using the method described in Ref. 10. Heats of adsorption were taken from Refs. 42 and 43, and vibrational frequencies were taken from Refs. 44 and 47.
[b]Reference 46.
[c]E_a from Refs. 45 and 48.
[d]References 44 and 47.
[e]This parallel vibration was actually determined from an EELS loss on the (100) terrace of a Ni(510) surface in Ref. 49.
[f]Reference 55.
[g]Binding energies calculated from heat of adsorption (ΔH_T) using the method described in Ref. 10. Heats of formation were taken from Refs. 43 and 57, and vibrational frequencies were taken from Refs. 11 and 51.
[h]References 50 and 52–54.
[i]E_a from Refs. 38 and 39.
[j]References 11 and 51.
[k]Reference 11.
[l]Reference 56.

all results in Table III and subsequent tables are converged with respect to relaxing the lattice atoms by the embedded-cluster method, both to confirm the effect of lattice motions and also to be consistent with results for interior sites and for the absorption and deabsorption processes, for which lattice motions are *very* important.

The interior stationary points O_I and $\ddagger_I$ were not considered in the parametrization as described above; however, since the corrections made for H interaction with Ni were primarily local ones that mostly affected A_{111} and $\ddagger_{111}$, they did not alter the energetics and frequencies of the interior stationary points. As a result, the calculation of these quantities closely match the EAM5 calculations, which are rea-

TABLE V. The (100), (111), (110), and (111) subsurface lattice structures. The first column lists the number of atoms in each plane of the lattice with the exposed (100) crystal face, the second column is for the lattice with the (111) face exposed, the third column is for the lattice with the (110) face exposed, and the fourth column is for the subsurface lattice calculations [also with the (111) crystal face exposed]. Numbers in parentheses are the numbers of atoms in the primary zone in each plane. The surface plane is denoted plane 1, the atomic plane immediately beneath the surface plane is denoted plane 2, etc.

Plane	(100)	(111)	(110)	Subsurface
1	132 (20)	136 (14)	98 (10)	141 (18)
2	126 (12)	125 (12)	95 (11)	137 (12)
3	124 (6)	123 (3)	92 (10)	136 (7)
4	112	108	93 (7)	129
5	98	90	84 (2)	114
6	78	71	83	91
7	60	42	76	69
8	44	3	68	42
9	16		58	7
10			49	
11			40	
12			29	
13			14	
total	790 (30)	698 (29)	879 (40)	866 (37)

sonably accurate compared to experiment, as confirmed by relaxed-lattice calculations reported below.

III. CALCULATIONS AND RESULTS

To construct embedded clusters, it is necessary to define the specific locations of the important stationary points of the hydrogen atom with respect to the lattice atoms. Given these locations, it is then necessary to decide which of the lattice atoms will be allowed to move in the simulation. For each of the processes studied, the locations of the stationary points from which the limits of the primary zone are extended are the reactant and product minimum-energy sites for the process. For the (110) calculations, the limits of the primary zone are extended from the A_{110} site. The construction of the lattices is outlined below.

We constructed one lattice for each of the three crystal faces, one lattice for the interior calculations, and one lattice for the (111) subsurface calculations. The first lattice, used for the H/Ni(100) calculations, exposes the (100) crystal face. The locations of the stationary points from which the limits of the primary zone are extended are two adjacent fourfold A_{100} sites, specifically the reactant and product sites of the hopping process. The lattice consists of 790 atoms, up to 38 of which are in the primary zone. The second lattice, used for the H/Ni(111) calculations, exposes the (111) crystal face. The locations of the stationary points from which the primary zone is extended are two adjacent threefold A_{111} sites, specifically the reactant and product sites of the hopping process. The lattice consists of 698 atoms, with up to 29 atoms in the primary zone. The third lattice is used for calculations on the (110) crystal face, and the location from
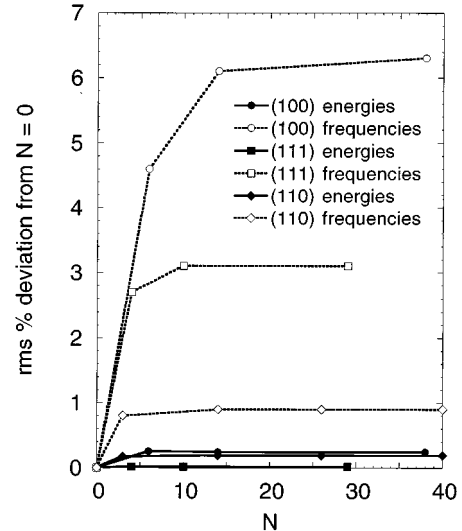
FIG. 6. Root-mean-squared percentage deviations from rigid lattice calculations of H binding energies and vibrational frequencies for H adsorbed at stationary points on Ni(100), Ni(111), and Ni(110) for increasing numbers of primary zone atoms. See text for details.

which the primary zone is extended is the A_{110} minimum-energy site. The lattice contains 879 atoms with up to 40 atoms in the primary zone. The fourth lattice, used for the H/Ni(interior) calculations, contains 1532 properly spaced Ni atoms that fit within two overlapping spheres of radii 15.3 Å centered at two adjacent O_I sites, and the primary zone consists of up to 52 atoms. The fifth lattice, used for the (111) subsurface calculations, also exposes the (111) crystal face. For this lattice, however, the locations of the stationary points from which the primary zone is extended are the $O_{S,111}$ site and the adjacent A_{111} site. The lattice contains 866 Ni atoms, with up to 37 Ni atoms in the primary zone. Table V gives a breakdown of the number of atoms in each atomic layer for the four lattices which expose a crystal face, and how many in each layer are in the primary zone. Note that this breakdown is not applicable to the interior lattice.

The size of the primary zone for each system has to be large enough that the energetic and dynamical results are converged with respect to N, the number of atoms in the primary zone. To determine the proper size of each primary zone, we examined the convergence of the results with respect to N. The six curves in Fig. 6 are plots of the root-mean-squared percentage deviation of the calculated H binding energies and vibrational frequencies of H adsorbed at sites on the three surfaces for various values of N from those obtained from a rigid surface ($N=0$) calculation. In particular, the curves are plots of the expression

$$\left[\sum_{i=1}^{I} \left(\frac{\alpha_{N,i} - \alpha_{0,i}}{\alpha_{0,i}} \right)^2 \Bigg/ I \right]^{1/2}, \qquad (20)$$

where $\alpha_{0,i}$ is a quantity calculated for a rigid surface ($N=0$), and $\alpha_{N,i}$ is the same quantity calculated for a system with N atoms in the primary zone. Figure 7 is a similar plot for the subsurface and interior site calculations. Note that, for each system, both a frequency convergence curve
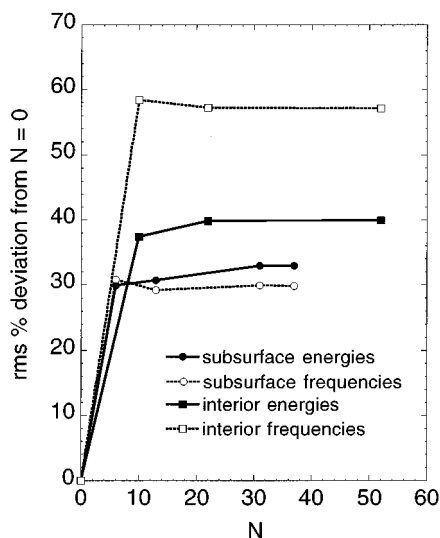
FIG. 7. Same as Fig. 6, except for H absorbed at stationary points in subsurface Ni and interior Ni. See text for details.

and a binding-energy convergence curve are given. Table VI gives the particular sites examined, and corresponding values of N and I used in expression (20) for the convergence curves for each system. The values of N examined for each case are dependent upon the structural symmetry of the lattice for that case, as discussed previously.[21] The value of I used in expression (20) is equal to the number of stationary points examined for the binding-energy convergence curves (i.e., one binding energy for each stationary point), and it is equal to three times the number of stationary points examined for the frequency convergence curves (i.e., three hydrogenic vibrations for each stationary point).

Figures 6 and 7 demonstrate that lattice motion is far more important for the subsurface and interior calculations than for the surface calculations. Specifically, lattice motion changes the binding energies by less than one-half of one percent for the surface calculations, but by 30–40 % in the subsurface and interior. Similarly, lattice motion changes the surface frequencies [those on the (100), (111), and (110) faces] by less than 6%, but it changes the subsurface and bulk frequencies by roughly 30–60 %. We note further that the tightly bound saddle points are more affected by lattice motion than the minimum-energy sites. Upon coupling to the vibrations of the lattice, the energy of the O_I site decreases by 3.4 kcal/mol, while that of the $\ddagger_I$ site decreases by 14.9

kcal/mol. The sum of the hydrogenic vibrational frequencies transverse to the reaction path mode at the O_I site decreases by 399 cm^{-1} (which corresponds to a 0.6-kcal/mol decrease in zero-point energy), while that at the $\ddagger_I$ site decreases by 2267 cm^{-1} (which corresponds to a 3.2-kcal/mol decrease in zero-point energy). Combining the energetic and frequency effects leads to a decrease in $\Delta V_a^{\ddagger G}$ [see Eq. (5)] for the interior diffusion process of 14.2 kcal/mol (11.5 kcal/mol from binding energy and 2.7 kcal/mol from frequencies) upon relaxation. A similar treatment with the $O_{S,111}$ and $\ddagger_{Ab,111}$ sites leads to a smaller (but still substantial) decrease in $\Delta V_a^{\ddagger G}$ for the deabsorption process of 4.5 kcal/mol upon relaxation. Since these relaxation effects are so pronounced for the subsurface and interior systems, particularly for the saddle points of the reaction paths studied for these systems, they have to be taken into account to carry out accurate dynamics calculations.

It is clear that the results are converged by the highest value of N used for each particular system, and in many cases the results are nearly converged by $N = 10$. A similar convergence was found for the rate constants. For example, rate constants calculated at the highest value of N were all within 6% of the rate constants calculated at the second-highest value on N.

Next we examine the variational and tunneling effects observed for the systems studied. Table VII gives the ratios of rate constants $k(T)$, calculated by CVT and CVT with tunneling corrections, to those calculated with conventional TST at a sample of temperatures. For the surface diffusion processes, variational effects are negligible [i.e., $k^{CVT}(T)/k^{TST}(T)$ equals 1.0]. For interior diffusion and deabsorption, however, the effects are substantial. For example, for interior diffusion, the CVT rate constants are lower than the TST rate constants by a factor of 2 at 600 K, and for deabsorption at the same temperature the CVT rates are lower than the TST rates by 27%. Variational effects become even more important at higher T. For three of these four processes, tunneling effects are very important, primarily at low temperatures. The important conclusion obtained from Table VII is that variational effects (especially for the interior and subsurface processes) and tunneling effects (especially at low temperatures) are important for a uniformly valid treatment of all the processes considered. Therefore, all rate constants and diffusion coefficients presented in this paper are calculated using CVT with tunneling corrections.

Using the lattices described above with EAM6 and version 6.1 of the POLYRATE code,[58] we calculated binding en-

TABLE VI. Specific sites examined for each system, and corresponding values of I used in expression (20) for the binding energy and frequency convergence curves. Values of N are the numbers of atoms in the primary zones considered in the convergence tests.

| System | Sites | I in expression (20) | | Values of N |
		Frequency curve	Binding energy curve	
H/Ni(100)	$A_{100}, \ddagger_{100}$	6	2	0, 6, 14, 38
H/Ni(111)	$A_{111}, \ddagger_{111}$	6	2	0, 4, 10, 29
H/Ni(110)	A_{110}	3	1	0, 3, 14, 26, 40
H/Ni(subsurface)	$O_{S,111}, \ddagger_{Ab,111}, \ddagger_{S,111}$	9	3	0, 6, 13, 31, 37
H/Ni(interior)	$O_I, Te_I, \ddagger_I$	9	3	0, 10, 22, 52

TABLE VII. Ratios of rate constants calculated by conventional TST, by CVT, and by CVT with tunneling (CVT/T) at a sample of temperatures. For the (100) and (111) diffusion processes, the tunneling method is SCTQ, and for interior diffusion and deabsorption, the tunneling method is SCT.

Temperature	$\dfrac{k^{\mathrm{CVT}}(T)}{k^{\mathrm{TST}}(T)}$	$\dfrac{k^{\mathrm{CVT}/T}(T)}{k^{\mathrm{CVT}}(T)}$	$\dfrac{k^{\mathrm{CVT}/T}(T)}{k^{\mathrm{TST}}(T)}$
(100) diffusion			
120 K	1.00	1.61	1.61
300 K	1.00	1.08	1.08
600 K	1.00	1.01	1.01
(111) diffusion			
120 K	1.00	176.14	176.14
300 K	1.00	1.64	1.64
600 K	1.00	1.21	1.21
interior diffusion			
120 K	0.67	1.33	0.89
300 K	0.59	1.05	0.62
600 K	0.46	1.00	0.46
1500 K	0.32	1.00	0.32
deabsorption			
120 K	0.83	6434.99	5341.04
300 K	0.81	2.74	2.22
600 K	0.73	1.01	0.74
1500 K	0.58	1.00	0.58

ergies, geometries, and vibrational frequencies of an H atom adsorbed at the A_{100}, $\ddagger_{100}$, A_{111}, $\ddagger_{111}$, and A_{110} sites and absorbed at the O_I, Te_I, $\ddagger_I$, H_I, $O_{S,111}$, $Te_{S,111}$, $\ddagger_{S,111}$, and $\ddagger_{Ab,111}$ sites. We also used CVT with the SCTQ and SCT tunneling approximations to examine the dynamics of H diffusion on (100) and (111) and in interior Ni, as well as H absorption into the (111) surface and the reverse process. Results of these calculations are given in Tables VIII–XV and Figs. 8–13, and they are discussed in Sec. IV.

IV. DISCUSSION

A. H/Ni(100) binding sites and surface diffusion

We compare several quantities to experiment[42–48] in Table VIII. First we consider quantities related to the equilibrium binding sites, which are fourfold sites on this crystal face. Binding energies (E, kcal/mol) are given with respect to the classical energy of a H atom infinitely separated from the surface. Hydrogen equilibrium heights above the surface (z, Å) are calculated as the perpendicular distance from the center of the H atom to the plane formed by the surface Ni atoms. Hydrogen-nickel equilibrium distances ($R_{\mathrm{H-Ni}}$, Å) are the distances between the center of the H atom and the center of one of the Ni nearest neighbors. The perpendicular hydrogenic vibrations ($\bar{v}_\perp$, cm^{-1}) are for the H atom stretching perpendicular to the surface plane. The parallel hydrogenic vibrations ($\bar{v}_\parallel$, cm^{-1}) are for H-atom motion parallel to the surface plane. Results for these quantities are all in very good agreement with experiment.

TABLE VIII. Binding energies E, hydrogen equilibrium heights z above the surface plane, hydrogen-nickel equilibrium nearest-neighbor distances $R_{\mathrm{H-Ni}}$, perpendicular H-Ni stretching vibrational frequencies $\bar{v}_\perp$, and doubly degenerate parallel H-Ni surface vibrational frequencies, $\bar{v}_\parallel$ for H on Ni(100) calculated by EAM5 and EAM6 compared to experiment.

Quantity	Experiment	EAM5 [a]	EAM6
	(A_{100})		
E (kcal/mol)	-64.5 ± 0.7 [b]	-64.76	-65.50
z (Å)	0.5 ± 0.1 [c]	0.50	0.49
$R_{\mathrm{H-Ni}}$ (Å)	$1.82-2.0$ [c]	1.83	1.84
$\bar{v}_\perp$ (cm^{-1})	$532-597$ [d]	753	751
$\bar{v}_\parallel$ (cm^{-1})		524	607
	$(\ddagger_{100})$		
E (kcal/mol)	$[-60\pm2$ [e]$]$	-60.76	-61.53
z (Å)		0.93	0.94
$R_{\mathrm{H-Ni}}$ (Å)		1.56	1.58
$\bar{v}_\perp$ (cm^{-1})		1270	1192
$\bar{v}_\parallel$ (cm^{-1})		449	569

[a]Reference 10.
[b]See footnote a in Table IV. The value given is an average of values calculated from the two experimental determinations of ΔH_T, which individually yield -64.5 ± 0.4 (Ref. 43) and -64.6 ± 0.6 (Ref. 42) kcal/mol.
[c]Reference 46.
[d]References 44 and 47.
[e]Estimation based on activation energies from Refs. 45 and 48. See the discussion at end of Sec. IV A.

Results for the diffusion coefficients of H on the Ni(100) crystal face are shown as an Arrhenius plot in Fig. 8 along with literature results. George, DeSantolo, and Hall[45] measured the diffusion coefficients using laser-induced thermal desorption, and performed the experiments at a hydrogen coverage θ of 0.12 ML. The same technique was used by Mullins *et al.*,[48] who measured the diffusion coefficients with approximately one monolayer of hydrogen atom coverage. Lin and Gomer[38] measured the diffusion coefficients with field-emission fluctuation and with hydrogen-atom coverages ranging from 0.25 to 0.95 ML. The results plotted in Fig. 8 that represent the work of Lin and Gomer are esti-

TABLE IX. High-temperature Arrhenius parameters for H diffusion on Ni(100) calculated by EAM5 and EAM6 compared to experiment. Activation energies E_a are given in kcal/mol, and pre-exponential factors D_0 are given in cm^2/s. Numbers in parentheses are powers of 10.

Quantity	Temperature	Experiment	EAM5 [a]	EAM6
E_a	$211-263$ [b]	4.0 ± 0.9 [b]	4.08	4.18
	$223-283$ [c]	3.5 ± 0.3 [c]	4.09	4.22
D_0	$211-263$ [b]	$4.5(-3)$ [b]	$4.6(-3)$	$2.8(-3)$
	$223-283$ [c]	$2.5(-3)$ [c]	$4.7(-3)$	$2.9(-3)$

[a]Reference 10.
[b]Reference 48.
[c]Reference 45.

TABLE X. Same as Table VIII, only for H on the Ni(111) surface.

Quantity	Experiment	EAM5 [a]	EAM6
	(A_{111})		
E (kcal/mol)	-66.2 ± 0.6 [b]	-62.42	-63.72
z (Å)	$1.05-1.25$ [c]	0.93	0.94
$R_{\text{H-Ni}}$ (Å)	$1.78-1.90$ [c]	1.72	1.72
$\bar{v}_\perp$ (cm^{-1})	$1121-1170$ [d]	1178	1075
$\bar{v}_\parallel$ (cm^{-1})	955 [e]	387	709
	($\ddagger_{111}$)		
E (kcal/mol)	$[-62\pm2$ [f]$]$	-61.60	-61.53
z (Å)		0.99	1.01
$R_{\text{H-Ni}}$ (Å)		1.60	1.62
$\bar{v}_\perp$ (cm^{-1})		1281	1489
$\bar{v}_\parallel$ (cm^{-1})		475	921

[a] Reference 10.

[b] See footnote g in Table IV. The value given is an average of values calculated from the two experimental determinations of ΔH_T, which individually yield -66.2 ± 0.3 (Ref. 43) and -66.2 ± 0.6 (Ref. 57) kcal/mol.

[c] References 50 and 52–54.

[d] References 11 and 51.

[e] Reference 11.

[f] See Sec. IV B for a discussion of the estimation of this quantity.

mated from the activation energies and preexponential factors reported in Ref. 38. Their results over this coverage range varied by less than one-half order of magnitude. Lee *et al.*[41] used linear optical diffraction techniques for their measurements, and the results representing their work plotted in Fig. 8 are for a hydrogen atom coverage of 0.7 ML. All of the theoretical work in the present paper was done in the single-adatom low-coverage limit. For the most part, agreement of theory and experiment is reasonably good for the magnitudes of the diffusion coefficients above about 90 K. Table IX gives the high-temperature Arrhenius parameters calculated in the current work. The results are in very good

TABLE XI. Binding energy E and frequencies of hydrogenic vibrations perpendicular to the surface plane ($\bar{v}_1$) and parallel to the surface plane ($\bar{v}_2$ and $\bar{v}_3$) for H adsorbed on the pseudothreefold binding site of the Ni(110) surface calculated by EAM5 and EAM6 and compared to experiment.

Quantity	Experiment	EAM5 [e]	EAM6
E (kcal/mol)	-64.7 ± 0.9 [b]	-63.1	-64.7
$\bar{v}_1$ (cm^{-1})	1100 [c]	1188	1053
$\bar{v}_2$ (cm^{-1})	870 [c]	208	604
$\bar{v}_3$ (cm^{-1})	635 [c]	316	599

[a] Reference 10.

[b] Binding energy calculated from heat of adsorption (ΔH_T) using the method described in Ref. 10. Heats of adsorption were taken from Refs. 43 and 66, and vibrational frequencies were taken from Ref. 63. The value given is an average of values calculated from the two experimental determinations of ΔH_T, which individually yield -65.0 ± 0.3 (Ref. 43) and -64.4 ± 0.6 (Ref. 66) kcal/mol.

[c] Reference 63.

agreement with the high-temperature experimental Arrhenius results of George, DeSantolo, and Hall[45] and Mullins *et al.*[48]

We next consider very low temperatures. Results at these temperatures depend strongly on the temperature at which the Arrhenius plot has its maximum curvature; this is called the transition temperature.[10] In previous work,[10] we showed that if a system can be qualitatively represented by a rigid surface with a harmonic reactant well, and the effective potential-energy barrier can be reasonably approximated by a parabola, then the transition temperature T_{tr} can be estimated by a simple function of the magnitude of the characteristic imaginary frequency describing that parabola. Specifically,

$$T_{\text{tr}} \cong \frac{hc|\vec{v}^\ddagger|}{2\pi k_B}, \tag{21}$$

where $|\bar{v}^\ddagger|$ is the magnitude of the imaginary frequency in wave numbers of an effective parabolic potential barrier. Fitting the V_a^G potential-energy barrier curve to a parabola on the average from $s \approx -1.30$ Å to $s \approx 1.30$ Å yields an imagi-

TABLE XII. Calculated values for the binding energies (kcal/mol) of H adsorbed at the A_{100}, A_{111}, and A_{110} sites by various theoretical methods compared to experiment.

Method	Reference	$E(A_{100})$	$E(A_{111})$	$E(A_{110})$
(Experiment)	Refs. 11, 42–44, 47, 51, 57, 63, and 66 [a]	-64.5 ± 0.7	-66.2 ± 0.6	-64.7 ± 0.9
EAM6	current work	-65.5	-63.7	-64.7
EAM5	Ref. 10	-64.8	-62.4	-63.1
DFT with nonlocal corrections	Mlynarski and Salahub (Ref. 73)	-67.1	-63.9	n.a. [b]
cluster model with bond preparation [c]	Panas *et al.* (Ref. 72)	-60.3 ± 3.0	-61.7 ± 4.5	n.a.
cluster model with bond preparation [d]	Panas *et al.* (Ref. 72)	-61.6	-57.2	n.a.
delocalized effective-medium theory	Lee and DePristo (Ref. 71)	-64.8	-57.4	-61.8
effective-medium theory	Nørskov and co-workers (Refs. 69 and 70)	-62	-62	-62
cluster model	Upton and Goddard (Ref. 68)	-70.1	-63.4	n.a.
tight binding	Fassaert and van der Avoird (Ref. 67)	-51.7	-49.4	n.a.

[a] See footnotes a and g in Table IV and footnotes b in Tables VIII, X, and XI.

[b] n.a. denotes not available.

[c] Average taken over all cluster sizes.

[d] Largest cluster size only.

TABLE XIII. Binding energies E, hydrogen-nickel equilibrium nearest-neighbor distances $R_{\text{H-Ni}}$, hydrogenic vibrational frequencies $\bar{v}$, Arrhenius activation energies E_a, and Arrhenius preexponential factors D_0 for absorbed H as calculated by EAM5 and EAM6 compared to experiment.

Quantity	Temperature	Experiment	EAM5 [a]	EAM6
(O_I)	0 K			
E (kcal/mol)		-53 ± 2 [b]	-55.21	-54.40
$R_{\text{H-Ni}}$ (Å)			1.82	1.82
$\bar{v}$ (cm^{-1})		800–850 [c]	858–860	857–859
(Te_I)	0 K			
E (kcal/mol)			-45.40	-44.81
$R_{\text{H-Ni}}$ (Å)			1.64	1.65
$\bar{v}$ (cm^{-1})			916–922	1251–1256
$(\ddagger_I)$	0 K			
E (kcal/mol)			-44.97	-43.25
$R_{\text{H-Ni}}$ (Å)			1.59	1.59
$\bar{v}$ (cm^{-1})			1124, 1120, 310i	1387, 1385, 695i
(H_I)	0 K			
E (kcal/mol)			-41.61	-38.59
$R_{\text{H-Ni}}$ (Å)			1.49	1.49
$\bar{v}$ (cm^{-1})			1720, 396i, 622i	1055, 278i, 526i
Arrhenius parameters for interior diffusion				
E_a (kcal/mol)	295–300 K		10.1	11.1
	300–627 K	9.4 ± 1 [d]	10.1	10.9
	627–1650 K	9.7 ± 1 [d]	10.0	10.2
D_0 (cm^2/s)	295–300 K		1.3 (-3)	1.3 (-3)
	300–627 K	4.8 (-3) [d]	1.4 (-3)	7.8 (-4)
	627–1650 K	6.9 (-3) [d]	1.2 (-3)	4.4 (-4)

[a]Reference 10.
[b]Binding energy calculated from heat of absorption ΔH_T using the method described in Ref. 10. Heats of adsorption were taken from Refs. 75 and 76, and vibrational frequencies were taken from Ref. 77.
[c]Reference 77.
[d]Reference 74.

nary frequency with a magnitude of 287 cm^{-1} (as compared to 305 cm^{-1} computed from d^2V_{MEP}/ds^2 at $s=0$). Using 287i cm^{-1} in Eq. (21) yields a transition temperature of 66 K, in good agreement with the value obtained by visual examination of the Arrhenius plot of the full dynamics calculations in Fig. 8. As in previous work,[10] the calculated transition temperature is lower than the experimental one.[38,41] The different locations of the transition temperatures among the various studies makes further comparison of the very-low-temperature diffusion coefficients and Arrhenius results (i.e., at and below the transition temperature) uninteresting,

but the results above the transition temperature are in very good agreement with experiment[45,48] and other theoretical[59] results, as discussed above.

Although there is no experimental measurement for the binding energy of a hydrogen atom at the saddle point on the (100) surface (or for any saddle point), values for $E(\ddagger_{100})$ can be estimated from the activation energies obtained by George, DeSantolo, and Hall[45] and Mullins *et al.*[48] because

TABLE XIV. Binding energies E (kcal/mol), and frequencies of hydrogenic vibration, $\bar{v}$ (cm^{-1}), for the $O_{S,111}$ and $\ddagger_{\text{Ab},111}$ subsurface sites, and classical and vibrationally adiabatic barrier heights ΔV_{MEP} and ΔV_a^G (kcal/mol) for H diffusing from the subsurface octahedral site to the surface A_{111} minimum energy site.

Quantity	$O_{S,111}$	$\ddagger_{\text{Ab},111}$
E	-55.39	-49.53
$\bar{v}$	862, 862, 820	1266, 1265, 970i
ΔV_{MEP}		5.86
ΔV_a^G		6.12

TABLE XV. Arrhenius activation energies E_a (kcal/mol) for H moving from the subsurface octahedral site to the surface A_{111} minimum-energy site (deabsorption), and for absorption from A_{111} to the subsurface octahedral site. All results are calculated with the CVT/SCT approximation.

T (K)	Deabsorption	Absorption
40–100	0.47	7.54
100–120	1.59	9.85
120–200	2.60	10.99
200–300	4.35	12.97
295–300	4.85	13.58
300–500	5.06	13.93
500–1000	5.10	14.27
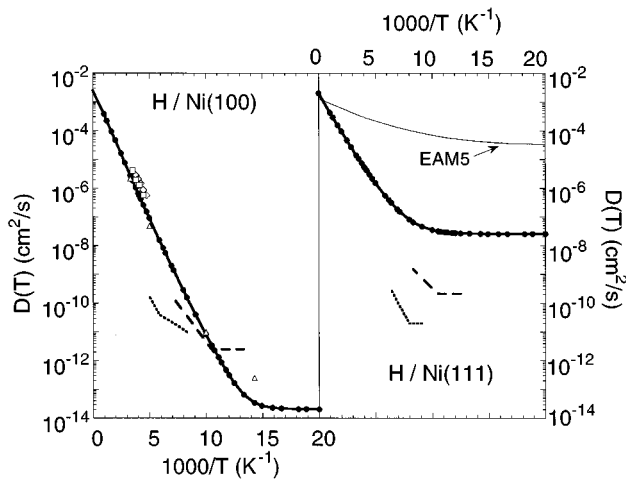
FIG. 8. Diffusion coefficients of H on Ni(100) and H on Ni(111) calculated in the current work compared to previous experimental and theoretical work. Solid circles represent current work, squares represent George, DeSantolo, and Hall (Ref. 45), diamonds represent Mullins *et al.* (Ref. 48), triangles represent Mattsson and co-workers (Ref. 59), short dashes represent Lee and co-workers (Refs. 39 and 41), and long dashes represent Lin and Gomer (Ref. 38).

these results are at a high enough temperature that the measured E_a is well approximated by our calculated $\Delta E_0^{\ddagger}$ [i.e., Eq. (7) is valid]. In particular, we note that Eq. (7) should be most valid if the temperature is simultaneously high enough that tunneling is negligible, and low enough that the assumptions of harmonic transition state theory do not break down. The results of Lin and Gomer[38] and by Lee *et al.*[41] are restricted to the very-low-temperature regime, where tunneling cannot be neglected even approximately. Thus $\Delta E_0^{\ddagger}$ is probably much better estimated from the higher-temperature experiments of George, DeSantolo, and Hall[45] and Mullins *et al.*[48] on (100). Using our saddle-point frequency calculations with the results of Ref. 48 yields a classical barrier height of 3.8 ± 0.3 kcal/mol. Combining this with $E(A_{100}) = -64.5 \pm 0.7$ kcal/mol (see Table VIII) yields a value of -60.7 ± 1.0 kcal/mol for $E(\ddagger_{100})$. A similar treat-
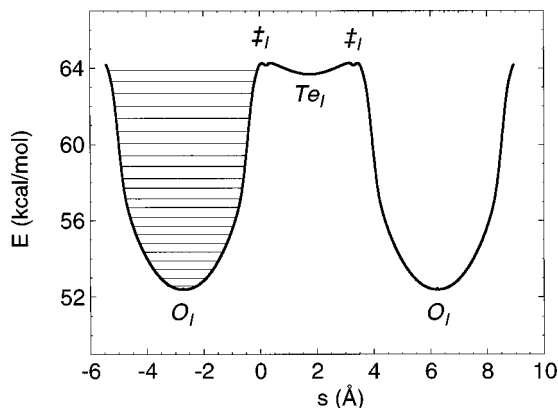
FIG. 9. Vibrationally adiabatic ground-state potential-energy curve for interior diffusion from one O_I site to another. Quantized reactant state energy levels are marked in the reactant octahedral well whose minimum occurs at $s = -2.7$ Å.
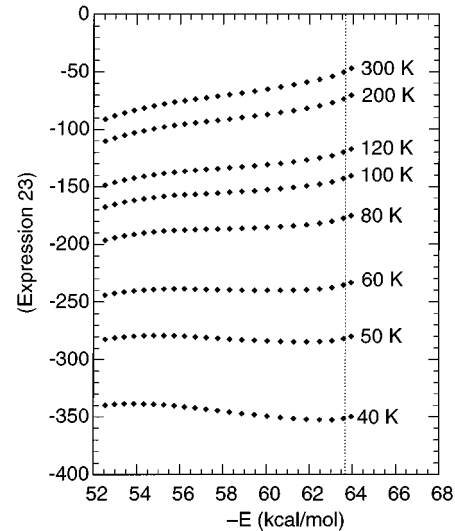
FIG. 10. Logarithm to the base 10 of the Boltzmann-weighted transmission probabilities, Eq. (23), from each of the quantized reactants states shown in Fig. 9 at various temperatures. The dashed vertical line at $E = 63.67$ kcal/mol is the vibrationally adiabatic ground-state energy of the Te_I site.

ment using the results of Mullins *et al.* yields a classical barrier height of 4.3 ± 0.9 kcal/mol and therefore $E(\ddagger_{100})$ equal to -60.2 ± 1.6 kcal/mol. Combining the two estimates gives -60 ± 2 kcal/mol, and Table VIII shows reasonable agreement of theory and experiment.

B. H/Ni(111) binding sites and surface diffusion

The results for the (111) crystal face are given in Table X and Fig. 8. Again we first consider results for the equilibrium binding site. Table X shows that $\bar{v}_{\parallel}$ for A_{111} shows a marked
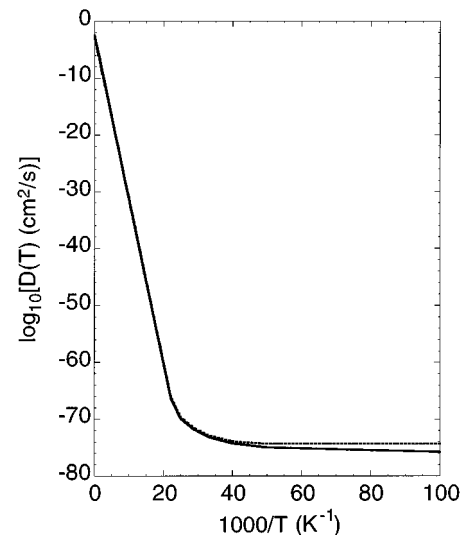
FIG. 11. Logarithm to the base 10 of coefficients for H interior diffusion in Ni. The solid line represents SCT calculations, and the dashed line represents SCTQ calculations. Arrhenius results presented in Table XIII are taken from SCT results. See the text for discussion.
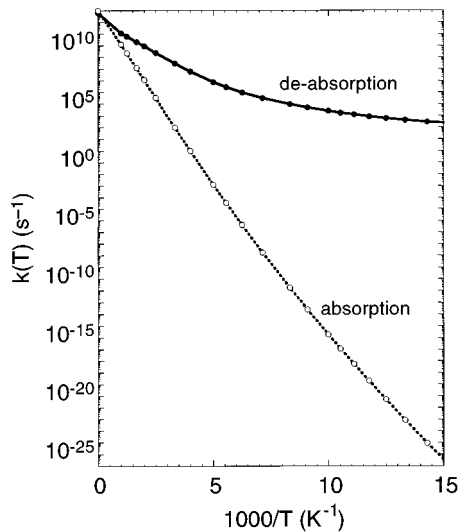
FIG. 12. Hopping rate constants of H for the absorption process from the A_{111} site atop the Ni(111) surface to a subsurface octahedral site below the Ni(111) surface ($O_{S,111}$), and for the reverse deabsorption process as calculated by the CVT/SCT method.

improvement of EAM6 over EAM5, but the equilibrium height above the surface plane is still too low.

Next we consider the surface diffusion process on (111). Fitting the V_a^G curve from $s \approx -0.67$ to 0.67 Å to a parabola yields an imaginary frequency of $426i$ cm^{-1} (as compared to $355i$ cm^{-1} calculated from $d^2 V_{MEP}/ds^2$ at $s=0$). Using the effective value of $426i$ cm^{-1} in Eq. (21) yields a transition temperature of 98 K, in close agreement with the full dynamics calculations given in the Arrhenius plot in Fig. 8, for which the temperature of maximum curvature is 115 K. Both calculated values are in excellent agreement with the experimental results of 100 (Ref. 38) and 125 K.[39]

The comparison to experiment for the (111) crystal face is complicated because, unlike the experimental results obtained for the (100) crystal face, those for the (111) face
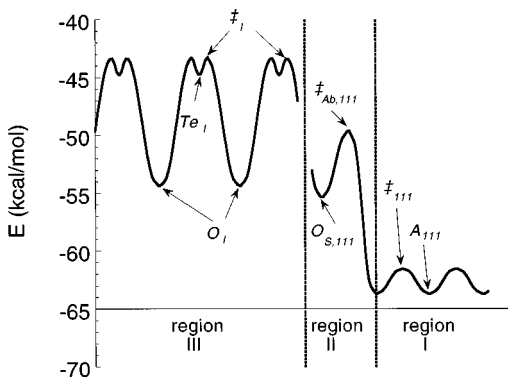
FIG. 13. Schematic diagram of the minimum-energy reaction path of a H atom diffusing across a (111) surface, absorbing into the surface, and diffusing in the interior. Region I represents the H atom diffusing across the (111) surface, region II represents absorption from the A_{111} site to the $O_{S,111}$ site beneath the surface, and region III represents H diffusion in the interior. Energy ordinate is with respect to a H atom infinitely far away from the Ni surface.

exhibit a sizable nonmonotonic H-atom coverage dependence. For example, the experiments of Lee et al.[39] were done at an approximate H-atom coverage of 0.3 ML. At this coverage, Lin and Gomer[38] measured an activation energy of approximately 3.6 kcal/mol. However, the latter researchers found that even over a relatively narrow range of H-atom coverages on the (111) surface (θ from 0.08 to 0.32 monolayer), the activation energy varied (somewhat erratically) between 2.6 ± 0.3 and 3.9 ± 0.3 kcal/mol, and showed a marked downward trend as coverage decreased from 0.2 ML to the lowest coverage examined, 0.08 ML. In contrast, recent studies by Wong, Lee, and Zhu[60] indicate an upward trend in the activation energy as coverage is decreased from 0.30 to 0.05 ML. Further, Lin and Gomer[38] also found erratic behavior for the pre-exponential factors, which varied from 9×10^{-5} to 4×10^{-2} cm^2/s for coverages from 0.08 to 0.32 ML.

Nevertheless, with these cautions we proceed to offer an attempt to estimate an ''experimental'' value for the binding energy of the saddle point on this surface, $E(\ddagger_{111})$, by using the activation energies measured by Lin and Gomer[38] and Lee et al.[39] and then applying the same treatment as used above to calculate $E(\ddagger_{100})$. We immediately run into the further difficulty that the experimental results for the (111) surface are not at high enough temperature to validate Eq. (7), and therefore the estimation of $E(\ddagger_{111})$ is not as straightforward as it is for $E(\ddagger_{100})$. Still, we will make an attempt to estimate $E(\ddagger_{111})$ here, because it can provide us with some insight into the accuracy of the (111) surface calculations of EAM6. Specifically, given that our calculated activation energy appears to be low compared to the low-temperature experimental data, we can estimate to what extent our predicted binding energy at the $\ddagger_{111}$ site might be in error.

As noted above, Lin and Gomer[38] measured activation energies on the (111) surface of approximately 3.3 ± 1.0 kcal/mol immediately above their transition temperature (for the temperature range of approximately 100–120 K) for H-atom coverages ranging from 0.8 to 0.32 ML. If we believe that our frequencies calculated for $\ddagger_{111}$ are reasonably accurate (which is a reasonable assumption since our calculated frequencies for A_{111} agree well with available experimental frequencies), and if Eq. (7) were valid for 100 K $< T < 120$ K on the (111) surface (this assumption is most likely inaccurate, as will be discussed shortly), then we could use our calculated frequencies and the activation energy of Lin and Gomer to obtain a value of 3.2 ± 1.0 kcal/mol for the classical barrier height. Combining this with $E(A_{111}) = -66.2 \pm 0.6$ kcal/mol (see Table X) would yield a value of 63.0 ± 1.6 kcal/mol for $E(\ddagger_{111})$. A similar treatment with the results of Lee et al.[30] would yield a value of 3.3 kcal/mol for the classical barrier height, and a value of 62.9 ± 0.6 kcal/mol for $E(\ddagger_{111})$.

The above treatment is not reliable because most likely $\Delta E_0^{\ddagger}$ is not a good estimation of E_a for the low-temperature ranges of the available experiments on the (111) surface because of the tunneling effect. We use the results for the (100) surface to estimate the size of the effect. Since the results of Lin and Gomer[38] indicate a transition temperature of approximately 100 K on both the (100) and (111) surfaces, the ratio of the rate constants k_{100} and k_{111}, measured at 120 K (the highest measured temperature common to both surfaces

in the experiment), combined with the known high-temperature activation energy on the (100) surface, can provide some insight into what a high-temperature activation energy would be on the (111) surface. Specifically, we assume

$$E_a(111, \text{ high } T) = E_a(100, \text{ high } T) + RT \ln \frac{K_{100}(T_C)}{k_{111}(T_C)} \tag{22}$$

where T_C is the highest temperature measured in common for both the (100) and (111) surfaces (120 K for the work of Lin and Gomer), R is the gas constant, E_a (111, high T) is the high-temperature activation energy for the (111) surface, and E_a (100, high T) is the same quantity for the (100) surface. Using $k_{100}(T_C)$ and $k_{111}(T_C)$ from Ref. 38 and E_a(100, high T) from Refs. 45 and 48 yields a value of 3.1 ± 0.9 kcal/mol for $E_a(111$, high $T)$. Then, assuming Eq. (7) is valid with this value of E_a, we estimate a classical barrier height of 4.0 ± 1.0 kcal/mol for (111) and a value of -62.2 ± 1.6 kcal/mol for $E(\ddagger_{111})$. Because of the indirect nature of this estimate, we increase the error estimate to ± 2 kcal/mol. These results, although tenuous, indicate that the $\ddagger_{111}$ site calculations of EAM6 are reasonably accurate, but the energy calculated for the A_{111} site is too high. We note that the apparent error in the binding energy at A_{111} is smaller for EAM6 than for EAM5, but any attempt to correct it further in the reparametrization of EAM6 resulted in unjustifiable damage to other predictions of the PEF.

We conclude this section with a discussion of future prospects for better characterizing the corrugation of the (111) surface. The discussion above makes it clear that a higher-temperature measurement of $D(T)$ would be especially helpful for this task. The field-emission fluctuation technique used by Lin and Gomer is only able[61] to measure diffusion coefficients as fast as 10^{-9} cm^2/s, and their measurements are already bordering that cutoff. It is unlikely, then, that this technique could be used to measure the diffusion coefficients at higher temperatures. The linear optical diffraction method used by Zhu is expected[62] to measure accurately diffusion coefficients as fast as 10^{-7} cm^2/s, and it would be very interesting to see higher-temperature results measured with the latter method for both the (100) and (111) surfaces. In particular, it would be interesting to see optical diffraction measurements of $D(T)$ for both the (100) and (111) surfaces over the same temperature range as studied by George, DeSantolo, and Hall and Mullins *et al.* on (100).

C. H/Ni(110) binding sites

The previous sections have shown that the EAM6 potential function accurately reproduces many experimental quantities relating to H on Ni(100) and Ni(111). Next, as a test of the universality of this PEF, we also examine a minimum-energy site on the Ni(110) surface. Unlike the (100) and (111) surfaces, the Ni(110) surface is known to reconstruct at high-H-atom coverages.[63-65] But at H-atom coverages below 1 ML, the surface is believed to remain unreconstructed.[63-65] At these low coverages, the H atom is proposed[63-65] to occupy the A_{110} site described in Sec. II A (see Fig. 3). There are three nondegenerate hydrogen vibrations at this site. One of them ($\bar{\nu}_1$) is a vibration perpendicular to the surface

plane; another ($\bar{\nu}_2$) is a vibration parallel to the Ni(110) surface plane, polarized parallel to the Ni atomic rows (see Fig. 3); and the last ($\bar{\nu}_3$) is a vibration parallel to the Ni(110) surface, polarized perpendicular to the Ni atomic rows.[63] Table XI gives the energetics and frequencies at this site calculated by EAM6 and compares them to experiment[43,63,66] and to those calculated by EAM5.[10] We note that the results calculated by EAM6 are in much better agreement with experiment than are those calculated by EAM5. The $\bar{\nu}_2$ parallel vibrational frequency is still low, but the error has been reduced by 60% as compared to EAM5. The overall agreement of the EAM6 predictions with experiment for the (110) crystal face is very encouraging, particularly because the (110) experimental results were not used in the fitting procedure. This agreement gives us additional confidence that EAM6 is a valid PEF for H interaction with Ni in a variety of environments.

D. Comparison of H/Ni(100), H/Ni(100), and H/Ni(111)

An interesting situation that deserves further discussion is the status of theoretical predictions of the relative binding energies of the A_{100}, A_{111}, and A_{110} sites. The experimental binding energy of H adsorbed at the A_{111} site is lower than that of H adsorbed at the A_{100} site; however, our potential function yields a lower binding energy for H adsorbed at A_{100}. Although the discrepancy with experiment has been lessened compared to EAM5, it is not removed. Attempts to improve the agreement of EAM6 with experiment further in this respect resulted in worse accuracy for other features of the potential function, such as barrier heights and frequencies, which are more important than absolute binding energies for dynamics calculations. Interestingly, we note that a wide variety of other theoretical methods have predicted the relative energies of these sites to be in the same order as predicted by our calculations; this is illustrated in Table XII. The experimental error bars in this table are based on the experimentalists' stated error bars on heats of adsorption and frequencies as well as the finite temperature range involved in the experiments. Possible systematic errors due to extrapolation to zero coverage and to surface defects are not included. Individual theoretical studies that calculate binding energies of both the A_{100} and A_{111} sites of H on Ni include the tight-binding extended Huckel calculations of Fassaert and van der Avoird,[67] the cluster model *ab initio* configuration interaction calculations of Upton and Goddard,[68] the effective medium theory calculations of Nørskov and co-workers,[69,70] the delocalized effective-medium theory calculations of Lee and DePristo,[71] the cluster-model calculations with bond preparation enhancements by Panas *et al.*,[72] and the density-functional treatments with nonlocal corrections of Mlynarski and Salahub.[73] Of these studies, only one[72] found a lower energy of H at the A_{111} site than at the A_{100} site, but in that case the stated uncertainty exceeds the energy difference between the faces. Table XII also includes results for (110) where these are available. We conclude that the relative binding energies on the various crystal faces are very difficult to explain theoretically.

E. H/Ni interior absorption sites and diffusion

For H in the interior, we again consider the equilibrium binding sites first. There is no experimental data for Te_I, but

for O_I there are experimental values for the binding energy and for the triply degenerate frequency of the hydrogen vibration. The comparison of theory and experiment[74–77] is given in Table XIII. Agreement is acceptable. We note from Tables VIII–XIII that although EAM6 is a very significant improvement over EAM5 for the H/Ni interaction, and even though most of the corrections made to the PEF were localized corrections affecting only the (111) crystal face, there are certain characteristics of the interior and (100) systems which are calculated *slightly* more accurately with EAM5 than with EAM6. This is because EAM5 was parametrized primarily with quantities involving the (100) crystal face, and the H-Ni nearest-neighbor distances are almost identical for A_{100} and O_I as well as for $\ddagger_{100}$ and $\ddagger_I$. However, EAM5 was *very* inaccurate for the (111) crystal face. Certainly, if we were to limit the reparametrization to quantities pertaining to the (111) crystal face, or even any one particular adsorption or absorption site, we could develop a PEF that reproduces such specific results better than EAM6 does; but it may not be a good PEF for general H/Ni interaction. The goal of this work was to create a PEF that predicts as many aspects of the H/Ni system (surface and interior) as accurately as possible in order to be able to apply it generally to H-Ni interactions. Although this meant allowing some of the quantities which were calculated very accurately by EAM5 for the (100) surface to deviate slightly more from the experimentally observed values with EAM6, the final values of the parameters were chosen to provide the best overall agreement with all quantities defining the H/Ni system.

The interior diffusion process is complex. Experimental measurements[74] of this process correspond to a H atom diffusing between two adjacent octahedral vacancies. Figure 4 shows that there are two distinct paths between two O_I sites. The first path, described in Sec. II, involves the H atom passing through a Te_I site en route to the destination O_I site. It can be written as

$$\mathrm{H}(O_I) \rightarrow \mathrm{H}(\ddagger_I) \rightarrow \mathrm{H}(Te_I) \rightarrow \mathrm{H}(\ddagger_I) \rightarrow \mathrm{H}(O_I) \quad \text{(process I)}.$$
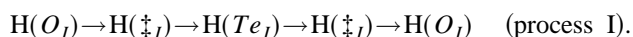
The second path is through the second-order saddle point H_I, directly joining the two O_I sites. This process can be written as

$$\mathrm{H}(O_I) \rightarrow \mathrm{H}(H_I) \rightarrow \mathrm{H}(O_I) \quad \text{(process II)}.$$
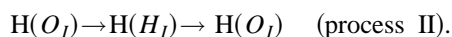
Process (II) is energetically less favorable because the energy of the second-order saddle point is 4.72 kcal/mol higher than the energy of $\ddagger_I$, and the calculated rate constant for this process is negligible compared to the rate constant of process (I) at all temperatures studied. As a result, process (I) provides the dominant reaction path for interior diffusion. The vibrationally adiabatic ground-state potential-energy curve [see Eq. (3)] for process (I) is shown in Fig. 9. The zero of energy for the ordinate is the classical energy (i.e., neglecting zero-point energy) of a lattice with 52 interior Ni atoms relaxed and the H atom infinitely far away.

Next, we consider the mechanism for process (I). If the lifetime of H at the Te_I site were long enough for the H atom to become thermalized there, then we would have to consider two individual kinetic steps in process (I), namely $\mathrm{H}(O_I) \rightarrow \mathrm{H}(\ddagger_I) \rightarrow \mathrm{H}(Te_I)$ and $\mathrm{H}(Te_I) \rightarrow \mathrm{H}(\ddagger_I) \rightarrow \mathrm{H}(O_I)$. However, the local minimum at Te_I is not very deep, and so

we treat process (I) as a single kinetic step with a double-maximum barrier rather than as two kinetic steps. In fact, since $V_{\mathrm{MEP}}(s)$ at $\ddagger_I$ is only 1.56 kcal/mol higher than that at Te_I, but 11.15 kcal/mol higher than that at O_I, there are appreciable tunneling contributions from energies below the vibrationally adiabatic energy level of H at the Te_I site.

We ran the tunneling calculations using both the SCTQ approximation and the SCT approximation. At most temperatures, the two sets of results were similar. When the system begins to settle into the ground state at very low temperatures, the two sets of results, as expected, begin to separate from one another, with the SCTQ results leveling off more rapidly. But this does not occur until below 40 K, which is well below the temperature range studied by experiment. The energy levels of the 22 quantized reactant states in the octahedral well are shown on the V_a^G curve in Fig. 9. Note that only the highest energy level E_{21} is above $V_a^G[s=s^R(Te_I)]$. The effect of tunneling from the bound energy levels at a given temperature can be quantified by calculating the Boltzmann distribution of the ground-state transmission probabilities at all energy levels E_n. Figure 10 plots the quantity

$$\log_{10}\left[P^G(E_n)\exp\left(\frac{-E_n}{k_B T} \right) \right] \qquad (23)$$

for a series of temperatures where $P^G(E_n)$ is the ground-state transmission probability at energy E_n. The vertical dotted line at 63.67 kcal/mol is $V_a^G[s=s^R(Te_I)]$ (see Fig. 7). We note that at all temperatures, the tunneling probability sharply increases for the energy level above $V_a^G[s=s^R(Te_I)]$. This is because above this energy, the system is tunneling through two thin barriers instead of one very wide one. Tunneling at energy levels below $V_a^G[s=s^R(Te_I)]$ is not negligible, and it becomes increasingly important at lower temperatures; however, our calculations show that the highest quantized energy level E_{21} contributes more to the tunneling rate constant than any other level for all temperatures above 50 K. However, since the quantized reactant state method only gives an approximation of the energy levels, and since there are a large number of very closely spaced energy levels in the reactant O_I well, we probably obtain a more robust calculation if the reaction coordinate is not quantized for calculations within the experimentally measured range. Figure 11 is a plot of the coefficients for interior H diffusion calculated at the SCT and SCTQ levels. The Arrhenius results given in Table XII are taken from the SCT level calculations.

F. H/Ni(111) absorption and deabsorption processes

Having obtained a PEF that we believe to be accurate for H interaction with Ni in a variety of environments, in this section we apply it to the important problems of absorption and deabsorption. Specifically, if the formation of methane from methyl radical indeed proceeds by the mechanism proposed by Marynard *et al.*[11] (see Sec. I), then an important part of this reaction is the process of a H atom moving from a subsurface site below the (111) surface to the A_{111} minimum-energy site where the methyl radical rests. This process is also of significant fundamental interest in its own

right. Using our general PEF, we can examine this process directly. The process of hydrogen passing from the first sub-surface layer to the surface is called deabsorption (not to be confused with desorption from the surface, which would be deadsorption) because it is the reverse of absorption.

Recall from Sec. II A that there are two distinct threefold minimum-energy sites on the (111) surface, and they are distinguished by the presence or absence of a Ni atom immediately below the site in the second atomic layer. While there is virtually no difference in the energies and vibrational frequencies of the H atoms adsorbed at these two sites, the distinction does become important for deabsorption and for determining at which site the hydrogenation of a methyl radical is most likely to occur. Given that the methyl radical rests in the threefold hollow A_{111} surface site, and given that the H atom prefers the octahedral vacancy to the tetrahedral vacancy (which we found to be true for the immediate subsurface interstitial sites as well as the higher symmetry deep interior sites), then there are two possible H-atom deabsorption pathways from subsurface to surface, namely

$$H(O_{S,111}) \rightarrow H(\ddagger_{S,111}) \rightarrow H(Te_{S,111}) \rightarrow H(\ddagger_{Ab,111}) \rightarrow H(A_{111})$$
$$\text{(process III)}.$$

and

$$H(O_{S,111}) \rightarrow H(\ddagger_{Ab,111}) \rightarrow H(A_{111}) \quad \text{(process IV)}.$$
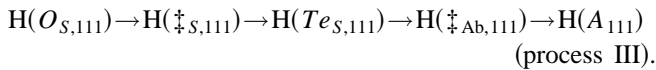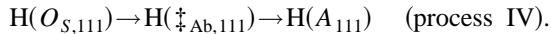
Notice that both processes are like interior diffusion processes that have been modified by truncating the solid at the (111) surface. If the lattice were not terminated by the (111) surface, the A_{111} site in process (III) would be an O_I site, and the one in process (IV) would be a Te_I site. The only difference between these two pathways is that process (III) passes through high-energy $\ddagger_{S,111}$ and $Te_{I,111}$ sites before reaching the surface. This makes process (III) less important than process (IV), and therefore we examine process (IV) in this work. Examining process (IV) also allows us to be consistent with the work of Yang, Whitten, and Markunas,[78] who studied the effects of subsurface H on surface-adsorbed CH_3. In their studies, the CH_3 is adsorbed on the tetrahedral extended A_{111} site, and the subsurface H atom is absorbed in the $O_{S,111}$ site.

Table XIV gives the binding energies and frequencies of the two subsurface sites in process (IV), as well as barrier heights for the diffusion process. Table XV gives Arrhenius activation energies for various temperature ranges of the forward (absorption) and reverse (subsurface-to-surface deabsorption) processes. Figure 12 is an Arrhenius plot of the rate constants for both directions. As with the results calculated for interior diffusion, all absorption and deabsorption results presented in Table XV and in Fig. 12 were calculated with the CVT/SCT approximation. We find that the rate constant of deabsorption process (IV) exceeds the interior diffusion rate constant of process (I) by factors of 4.3×10^7, 2.2×10^4, and 6.6×10^2 at 200, 300, and 400 K, respectively. These results should be of use for future models of the Ni-catalyzed methane formation.

V. SUMMARY

We have presented an improved EAM potential-energy surface, called EAM6, which yields realistic values for most

features of H interaction with Ni(100), Ni(111), and Ni(110), and for H diffusion in Ni. The potential function is especially designed to provide useful accuracy for diffusion barriers, vibrational frequencies, interatomic distances, and reaction dynamics. The parametrization of EAM6 was accomplished in three steps. First, we assumed the previous form of the effective nuclear charge on Ni, $Z_{Ni}(R_{\alpha\alpha'})$, and we adjusted the Ni embedding function $F_{Ni}(\bar{\rho}_\alpha)$ to agree with interior properties of Ni (with no H atom present) using the universal energy function of Rose $et\ al.$[30] Second, we assumed additional functional forms for the effective nuclear charge on H, $Z_H(R_{\alpha\alpha'})$, and the H embedding function $F_H(\bar{\rho}_\alpha, \hat{\rho}_\alpha^{(1)}, \hat{\rho}_\alpha^{(2)})$, so as to minimize as much as possible the deviation of several H-atom surface energetic quantities from their experimental and calculated values. Third, we added nonlocal density effects to the H embedding function to more clearly distinguish the surface stationary points, and we adjusted this function to further minimize the deviation from experiment. Although the PEF accurately reproduces most experimental quantities describing an H atom interacting with the (100) and (110) crystal faces of Ni as well as those describing an H atom absorbed in interior Ni, for (111) it apparently predicts too small a binding energy at the three-fold site.

An interesting conclusion drawn from the parametrization effort is that lattice relaxation is much more important for understanding the energetics and dynamics at subsurface and interior sites than it is for understanding them at surface sites. For example, hydrogenic frequencies at interior saddle points decrease by factors of nearly 2 upon coupling of hydrogenic motions to the metallic lattice motions, and the vibrationally adiabatic barrier height decreases by over 14 kcal/mol. Nevertheless we were able to obtain good convergence by the embedded cluster approach with 10–20 movable atoms.

The results obtained for the Ni(111) crystal face, subsurface, and interior Ni in the present study are summarized in Fig. 13. For this figure, region I represents the diffusion of the H atom along the (111) surface. Region II represents the absorption of the H atom into the metal to a subsurface octahedral site. Region III represents interior diffusion far beneath the surface. The curves represent the classical potential energy of the reaction path.

Since the results presented in this paper are all in reasonable agreement with experiment, and since the potential functions are smooth and well behaved between low-density surface-sensitive regions and high-density interior-sensitive regions, EAM6 should be useful for a broad range of modeling applications involving systems in intermediate surrounding atomic densities. As an example, we have predicted rate constants for passage of H atoms from the Ni(111) surface to the layer below the surface and for the reverse process.

[1] *Many-Atom Interactions in Solids*, edited by R. M. Nieminen, M. J. Puska, and M. J. Manninen (Springer-Verlag, Berlin, 1990).

[2] M. S. Daw and M. I. Baskes, Phys. Rev. B **29**, 6443 (1984).

[3] S. M. Foiles, M. I. Baskes, and M. S. Daw, Phys. Rev. B **33**, 7983 (1986).

[4] S. M. Foiles, M. I. Baskes, C. F. Melius, and M. S. Daw, J. Less-Common Met. **130**, 465 (1987).

[5] M. S. Daw, Phys. Rev. B **39**, 7441 (1989).

[6] M. S. Daw, S. M. Foiles, and M. I. Baskes, Mater. Sci. Rep. **9**, 251 (1993).

[7] T. N. Truong, D. G. Truhlar, and B. C. Garrett, J. Phys. Chem. **93**, 8227 (1989).

[8] T. N. Truong and D. G. Truhlar, J. Phys. Chem. **94**, 8262 (1990).

[9] B. M. Rice, B. C. Garrett, M. L. Koszykowski, S. M. Foiles, and M. S. Daw, J. Chem. Phys. **92**, 775 (1990); **100**, 8556 (1994)(E).

[10] S. E. Wonchoba, W.-P. Hu, and D. G. Truhlar, Phys. Rev. B **51**, 9985 (1995).

[11] K. J. Maynard, A. D. Johnson, S. P. Daley, and S. T. Ceyer, Faraday Discuss. Chem. Soc. **91**, 437 (1991).

[12] D. G. Truhlar and B. C. Garrett, Acc. Chem. Res. **13**, 440 (1980).

[13] D. G. Truhlar and B. C. Garrett, Annu. Rev. Phys. Chem. **35**, 159 (1984).

[14] D. G. Truhlar, A. D. Isaacson, and B. C. Garrett, in *Theory of Chemical Reaction Dynamics*, edited by M. Baer (CRC Press, Boca Raton, FL, 1985), pp. 65–137.

[15] D. G. Truhlar and B. C. Garrett, J. Chem. Phys. **84**, 365 (1987).

[16] S. C. Tucker and D. G. Truhlar, in *New Theoretical Methods for Understanding Organic Reactions*, edited by J. Bertran and I. G. Csizmadia (Kluwer, Dordrecht, 1989), pp. 291–346.

[17] S. E. Wonchoba, W.-P. Hu, and D. G. Truhlar, in *Theoretical and Computational Approaches to Interface Phenomena*, edited by H. L. Sellers and J. T. Golab (Plenum, New York, 1994), p. 1.

[18] D.-h. Lu, T. N. Truong, V. S. Melissas, G. C. Lynch, Y.-P. Liu, B. C. Garrett, R. Steckler, A. D. Isaacson, S. N. Rai, G. Hancock, J. G. Lauderdale, T. Joseph, and D. G. Truhlar, Comput. Phys. Commun. **71**, 235 (1992).

[19] J. G. Lauderdale and D. G. Truhlar, J. Chem. Phys. **84**, 1843 (1986).

[20] A. F. Voter and J. D. Doll, J. Chem. Phys. **80**, 5832 (1984); S. M. Valone, A. F. Voter, and J. D. Doll, Surf. Sci. **155**, 687 (1985).

[21] S. E. Wonchoba and D. G. Truhlar, J. Chem. Phys. **99**, 9637 (1993).

[22] D. G. Truhlar, F. B. Brown, R. Steckler, and A. D. Isaacson, in *The Theory of Chemical Reaction Dynamics*, edited by D. C. Clary (Reidel, Dordrecht, 1986), p. 285.

[23] B. C. Garrett, M. J. Redmon, R. Steckler, D. G. Truhlar, K. K. Baldridge, D. Bartol, M. W. Schmidt, and M. S. Gordon, J. Phys. Chem. **92**, 1476 (1988).

[24] R. A. Marcus, J. Chem. Phys. **49**, 2610 (1968).

[25] I. Shavitt, J. Chem. Phys. **49**, 4048 (1968).

[26] D. G. Truhlar and A. Kuppermann, J. Am. Chem. Soc. **93**, 1840 (1971).

[27] K. Fukui, in *The World of Quantum Chemistry*, edited by R. Daudel and B. Pullman (Reidel, Dordrecht, 1974), p. 113.

[28] H. F. Schaefer III, Chem. Brit. **11**, 227 (1975).

[29] D. G. Truhlar, J. Chem. Educ. **55**, 309 (1978).

[30] J. H. Rose, J. R. Smith, F. Guinea, and J. Ferrante, Phys. Rev. B **29**, 2963 (1984).

[31] C. Kittel, *Introduction to Solid State Physics*, 6th ed. (Wiley, New York, 1986).

[32] *Metal Reference Book*, 5th ed., edited by C. J. Smith (Butterworths, London, 1976), p. 186.

[33] *Vacancies and Interstitials in Metals*, edited by A. Seeger, D. Schumacher, W. Schilling, and J. Diehl (North-Holland, Amsterdam, 1970), p. 36; H. Bakker, Phys. Status Solidi **28**, 569 (1968).

[34] R. A. Johnson, Phys. Rev. **145**, 423 (1965).

[35] A. A. Mamalui, T. D. Ostinskaya, V. A. Pervakov, and V. I. Khomkevich, Fiz. Tverd. Tela (Leningrad) **10**, 2892 (1968) [Sov. Phys. Solid State **10**, 2290 (1969)].

[36] W. Wycisk and M. Feller-Kniepmeier, J. Nucl. Mater. **69&70**, 616 (1978).

[37] G. Simmons and H. Wang, *Single Crystal Elastic Constants and Calculated Aggregate Properties: A Handbook* (MIT Press, Cambridge, MA, 1971).

[38] T.-S. Lin and R. Gomer, Surf. Sci. **225**, 41 (1991).

[39] A. Lee, X. D. Zhu, A. Wong, L. Deng, and U. Linke, Phys. Rev. B **48**, 11 256 (1993).

[40] W. H. Press, S. A. Teukolsky, W. T. Vetterling, and B. P. Flannery, *Numerical Recipes in FORTRAN*, 2nd ed. (Cambridge University Press, Ithaca, NY, 1992).

[41] A. Lee, X. D. Zhu, L. Deng, and U. Linke, Phys. Rev. B **46**, 15 472 (1992).

[42] J. Lapujoulade and K. S. Neil, Surf. Sci. **35**, 288 (1973).

[43] K. Christmann, O. Schober, G. Ertl, and H. Neumann, J. Chem. Phys. **60**, 4528 (1974).

[44] S. Andersson, Chem. Phys. Lett. **55**, 185 (1978).

[45] S. M. George, A. M. DeSantolo, and R. B. Hall, Surf. Sci. **159**, L425 (1985).

[46] I. Stensgaard and F. Jakobsen, Phys. Rev. Lett. **54**, 711 (1985).

[47] P.-A. Karlson, A.-S. Mårtensson, S. Andersson, and P. Nordlander, Surf. Sci. **175**, L759 (1986).

[48] D. R. Mullins, B. Roop, S. A. Costello, and J. M. White, Surf. Sci. **186**, 67 (1987).

[49] A.-S. Mårtensson, C. Nyberg, and S. Andersson, Surf. Sci. **205**, 12 (1988).

[50] K. Christmann, R. J. Behm, G. Ertl, M. A. Van Hove, and W. H. Weinberg, J. Chem. Phys. **70**, 4168 (1979).

[51] W. Ho, N. J. DiNardo, and E. W. Plummer, J. Vac. Sci. Technol. **17**, 134 (1980).

[52] R. R. Cavanagh, R. D. Kelley, and J. J. Rush, J. Chem. Phys. **77**, 1540 (1982).

[53] K. Mortensen, F. Besenbacher, I. Stensgaard, and J. R. Wampler, Surf. Sci. **205**, 433 (1988).

[54] G. Gross and K. H. Rieder, Surf. Sci. **241**, 33 (1991).

[55] T. H. Upton and W. A. Goddard, Phys. Rev. Lett. **42**, 472 (1979).

[56] H. Yang and J. L. Whitten, J. Chem. Phys. **98**, 5039 (1993).

[57] J. Lapujoulade and K. S. Neil, J. Chem. Phys. **57**, 3535 (1972).

[58] D.-h. Lu, T. N. Truong, V. S. Melissas, G. L. Lynch, Y.-P. Liu, B. C. Garrett, R. Steckler, A. D. Isaacson, S. N. Rai, G. C. Hancock, J. G. Lauderdale, T. Joseph, and D. G. Truhlar, Comput. Phys. Commun. **71**, 235 (1992); R. Steckler, W.-P. Hu, Y.-P. Liu, G. C. Lynch, B. C. Garrett, A. D. Isaacson, D.-h. Lu, V. S. Melissas, T. N. Truong, S. N. Rai, G. C. Hancock, J. G. Lauderdale, T. Joseph, and D. G. Truhlar, QCPE Bull. **15**, 40 (1995).

[59] T. R. Mattsson, U. Engberg, and G. Wahnström, Phys. Rev. Lett. **71**, 2615 (1993); T. R. Mattsson and G. Wahnström, Phys. Rev. B **51**, 1885 (1995).

[60] A. Wong, A. Lee, and X. D. Zhu, Phys. Rev. B **51**, 4418 (1995).

[61] R. Gomer, Rep. Prog. Phys. **53**, 917 (1990).

[62] X. D. Zhu, Mod. Phys. Lett. B **6**, 1217 (1992).

[63] B. Voigtländer, S. Lehwald, and H. Ibach, Surf. Sci. **208**, 113 (1989).

[64] C. D. Roux, H. Bu, and J. W. Rabalais, Surf. Sci. **259**, 253 (1991).

[65] H. Bu, C. D. Roux, and J. W. Rabalais, Surf. Sci. **271**, 68 (1992).

[66] J. Lapujoulade and K. S. Neil, J. Chim. Phys. **70**, 798 (1973).

[67] D. J. M. Fassaert and A. van der Avoird, Surf. Sci. **55**, 291 (1976); **55**, 313 (1976).

[68] T. H. Upton and W. A. Goddard III, CRC Crit. Rev. Solid State Mater. Sci. **10**, 261 (1981).

[69] J. K. Nørskov, Phys. Rev. Lett. **48**, 1620 (1982).

[70] P. Nordlander, S. Holloway, and J. K. Nørskov, Surf. Sci. **136**, 59 (1984).

[71] C.-Y. Lee and A. E. DePristo, J. Chem. Phys. **85**, 4161 (1986).

[72] I. Panas, J. Schüle, P. Siegbahn, and U. Wahlgren, Chem. Phys. Lett. **149**, 265 (1988).

[73] P. Mlynarski and D. R. Salahub, J. Chem. Phys. **95**, 6050 (1991).

[74] *Hydrogen in Metals*, edited by G. Alefeld and J. Völkl (Springer-Verlag, Berlin, 1978), Vols. I and II.

[75] S. W. Stafford and R. B. McLellan, Acta Metall. **22**, 1463 (1974).

[76] R. B. McLellan and W. A. Oates, Acta Metall. **21**, 181 (1973).

[77] A. D. Johnson, K. J. Maynard, S. P. Daley, Q. Y. Yang, and S. T. Ceyer, Phys. Rev. Lett. **67**, 927 (1991).

[78] H. Yang, J. L. Whitten, and R. J. Markanus, Surf. Sci. Rep. **75**, 12 (1994).